Measurements of Form and Frictional Drags over a Rough Topographic Bank

H. W. WIJESEKERA, E. JAROSZ, W. J. TEAGUE, AND D. W. WANG

Naval Research Laboratory, Stennis Space Center, Mississippi

D. B. FRIBANCE

Coastal Carolina University, Conway, South Carolina

J. N. MOUM AND S. J. WARNER

Oregon State University, Corvallis, Oregon

(Manuscript received 18 October 2013, in final form 10 June 2014)

ABSTRACT

Pressure differences across topography generate a form drag that opposes the flow in the water column, and viscous and pressure forces acting on roughness elements of the topographic surface generate a frictional drag on the bottom. Form drag and bottom roughness lengths were estimated over the East Flower Garden Bank (EFGB) in the Gulf of Mexico by combining an array of bottom pressure measurements and profiles of velocity and turbulent kinetic dissipation rates. The EFGB is a coral bank about 6 km wide and 10 km long located at the shelf edge that rises from 100-m water depth to about 18 m below the sea surface. The average frictional drag coefficient over the entire bank was estimated as 0.006 using roughness lengths that ranged from 0.001 cm for relatively smooth portions of the bank to 1–10 cm for very rough portions over the corals. The measured form drag over the bank showed multiple time-scale variability. Diurnal tides and low-frequency motions with periods ranging from 4 to 17 days generated form drags of about 2000 N m^{-1} with average drag coefficients ranging between 0.03 and 0.22, which are a factor of 5–35 times larger than the average frictional drag coefficient. Both linear wave and quadratic drag laws have similarities with the observed form drag. The form drag is an important flow retardation mechanism even in the presence of the large frictional drag associated with coral reefs and requires parameterization.

1. Introduction

Roughness elements and rough bathymetric features generate resistance to flow through skin friction and pressure anomalies, which are referred to as frictional drag (or frictional skin drag) and pressure drag (or form drag), respectively. Frictional drag is a tangential stress on the surface caused by the molecular diffusion of momentum across a velocity interface (Schlichting 1962) and also applies to heat, salt, and other scalars. This is primarily true for hydrodynamically smooth flows where the bulk of the force on the surface is by viscosity because pressure forces are negligible. However in rough flows, where the roughness elements are larger than the molecular sublayer, the force on the surface is transmitted mainly by the pressure forces on roughness elements, and the force is parameterized as frictional drag (Schlichting 1962; Tennekes and Lumley 1972). The frictional drag depends strongly on the hydrodynamic roughness or the roughness Reynolds number (e.g., Nikuradse 1950). The parameterization of frictional drag is typically derived from inertial or wall boundary layer theory (e.g., Tennekes and Lumley 1972; Stull 1988) and has been applied in both atmosphere and ocean models (Blumberg and Mellor 1987; Hodur 1997).

Form drag is related to the dynamic pressure differences across an obstacle arising from upstream blocking and separation of flow and formation of eddies, hydraulic jumps, and lee-wave disturbances downstream of the obstacle (Gill 1982; Smith 1989; Baines 1995). The nature of the flow depends on the governing parameters such as Froude number Fr, nondimensional obstacle height h_n and width a_n, and mode number K. For single-layer hydraulic

Corresponding author address: Hemantha W. Wijesekera, Naval Research Laboratory, 1009 Balch Blvd., Stennis Space Center, MS 39529.
E-mail: hemantha.wijesekera@nrlssc.navy.mil

DOI: 10.1175/JPO-D-13-0230.1

flows, $\mathrm{Fr} = U_0/\sqrt{gD}$, where U_0 is the flow speed of the layer, g is the gravitational acceleration, and D is the flow depth.

In stratified depth-limited flows, the nondimensional height of the bank or nonlinearity parameter h_n, the nondimensional width a_n, the mode number K, the aspect ratio of the bank h_0/L, and the height parameter h_0/D are used as nondimensional parameters to describe the nature of the flow, where $h_n = N_0 h_0/U_0$, $a_n = N_0 a_0/U_0$, and $K = N_0 D/(\pi U_0)$; N_0 and U_0 are characteristic scales of stratification and flow speed of the water column, h_0 is the height of the bank, D is the flow depth, L is the width of the bank, and a_0 is the half-width scale (Hunt and Snyder 1980; Smith 1980; Durran 1986; Baines 1995; Vosper et al. 1999). For $h_n < 1$ and $K < 1$, the flow moves over the bank (nonblocked flow), and for $h_n > 1$ and $K > 1$, the flow moves around the bank (blocked flow) (e.g., Hunt and Snyder 1980). In the presence of background stratification, the flow over obstacles generates internal gravity waves and in turn transports horizontal momentum vertically (when $h_n < 1$). The resulting wave momentum flux generates a form drag to the background flow that is also referred to as wave drag (e.g., Durran 1986, 1990; Smith 1989). Form drag is patchy in space due to the spatial variability of the bottom topography, unlike frictional drag that occurs on the entire bottom surface.

Form drag for airflow over mountains has been studied extensively in both field observations and numerical simulations with special emphasis on improving the parameterization of mountain wave drag (Smith 1978, 1979, 1980; Bougeault et al. 1990; Durran 1990; Clark and Miller 1991; Olafsson and Bougeault 1996; Doyle and Jiang 2006). Several decades of mountain wave studies were beneficial to the estimation of mountain wave drag based mainly on linear internal wave solutions. Such parameterizations have resulted in substantial improvements in current weather prediction models (e.g., Kim and Arakawa 1995; Wood et al. 2001; Kim et al. 2003). Form drag has been computed for both small and large atmospheric mountain ranges. On a smaller scale, Smith (1978) evaluated pressure drag in the Blue Ridge Mountains in the United States using several microbarographs across the ridge, resolving the pressure field over the ridge similar to the oceanic observations made by Warner et al. (2013). However, for most atmospheric observations, measurements of pressure over mountain terrains are quite sparse, as the instruments cannot cover the entire mountain range. Hafner and Smith (1985) used a limited number of microbarographs over the European Alps to evaluate the pressure drag by assuming lateral pressure gradients were constant; even though these observations do not resolve the entire pressure field over the complex terrains, a rough estimate of form drag was obtained. In recent mountain wave experiments such as the Terrain-Induced Rotor Experiment (T-REX; Grubisic et al. 2008) microbarographs measurements were used, but a few microbarographs measurements are not sufficient to compute the pressure drag directly. Instead, pressure measurements have been used to obtain information on internal lee waves.

In the ocean, observational studies of form drag are very limited (e.g., Nash and Moum 2001; Warner et al. 2013). Form drag acts on the entire water column over the topographic feature and leads to the generation of mixing and turbulence, eddies, and internal waves away from the bottom (e.g., Polzin et al. 1997; Jayne and St. Laurent 2001; Pawlak et al. 2003; Garrett and Kunze 2007). Some aspects of topographic–tidal flow interaction and formation of lee waves have been studied analytically and numerically using nonhydrostatic models (Bell 1975; Nakamura et al. 2000; Khatiwala 2003; Legg and Huijts 2006). Several numerical studies have been conducted to examine the dynamics of flows over small banks (e.g., Lamb 1994; Skyllingstad and Wijesekera 2004; Seim et al. 2012). Lamb (1994) and Skyllingstad and Wijesekera (2004) reported qualitatively comparable results to the theoretical and laboratory results of Long (1955) and Baines (1979) for a similar dynamical parameter range ($1 < K < 2$ and $a_n < 10$). Skyllingstad and Wijesekera (2004) noted for $K < 1$, a substantial reduction in the wave drag compared to a no-slip boundary when bottom roughness was introduced. Ocean circulation models do not have form drag parameterizations (Blumberg and Mellor 1987; Oke et al. 2002), mainly due to lack of information on the magnitude and spatial distribution of form drag, although some attempts have been made to approximate wave drag from linear theory (Nikurashin and Ferrari 2011).

The total form drag consists of different components that involve isopycnal displacement (referred as ''internal'') and surface tilt (referred as ''external''; e.g., McCabe et al. 2006). Different components of form drag over coastal banks and ridges were examined by several investigators (Moum and Nash 2000; Nash and Moum 2001; Edwards et al. 2004; McCabe et al. 2006). Warner et al. (2013) were first to measure the total form drag from high-precision pressure sensors (referred to as Ppods; Moum and Nash 2008) deployed over Three Tree Point (TTP), a headland in Puget Sound, Washington. Warner et al. (2013) reported that the form drag coefficient is at least one order of magnitude larger than the frictional drag coefficient at the bottom.

In the following, we compute both form drag and frictional drag from in situ measurements collected over the East Flower Garden Bank (EFGB) on the Texas–Louisiana shelf (Fig. 1) as part of projects sponsored by the Naval Research Laboratory [NRL; Mixing Over

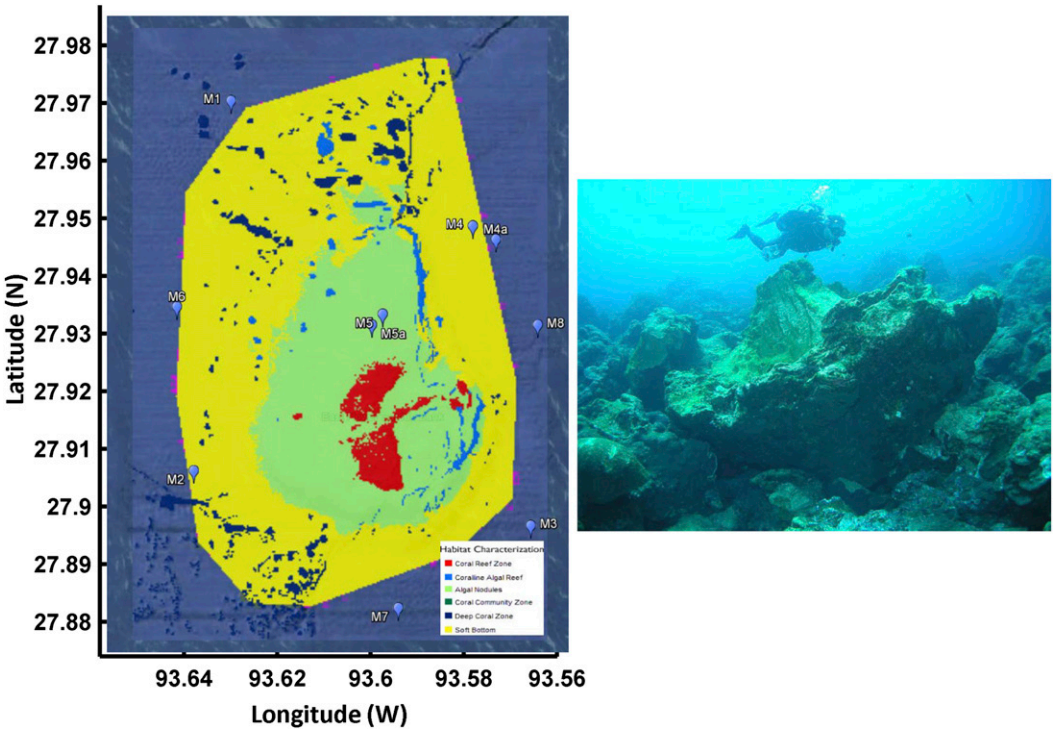

FIG. 1. (left) Habitat characterization map of the EFGB, along with mooring locations. The edge of the habitat map is the boundary of the marine sanctuary. Habitat characterization was provided by NOAA (available at http://www.ncddc.noaa.gov/website/google_maps/FGB/mapsFGB.htm). Red, blue, light green, green, dark blue, and yellow regions denote coral reefs, coralline algal reef, algal nodules, coral community zone, and soft bottom, respectively. Barny moorings (M1–M8, M4a, and M5a) are also marked on the map. (right) Roughness elements associated with corals. A diver was examining the underside of a dislodged coral head after Hurricane Ike in September 2008. Photographer: E. Hickerson, Flower Garden Banks National Marine Sanctuary. This image is part of a larger collection of sanctuary media found online (at https://marinelife.noaa.gov/media_lib).

Rough Topography (MORT)] and by the Bureau of Ocean Energy Management [BOEM; Currents over Banks (COB)]. As described below, the flow over the EFGB consists of $h_n \gg 1$, $K \gg 1$, and $a_n \sim O(100)$ along with large bottom roughness lengths ($z_0 \sim 1$–10 cm). This parameter regime belongs to nonlinear, hydrostatic, blocking flows, and there is no theoretical prediction of the form drag. Main objectives are to quantify the magnitude and temporal variability of the form drag through bottom pressure measurements collected from June to December 2011 and to quantify roughness lengths and associated frictional drag coefficients from microstructure and velocity profiles collected during an intensive observational period in June 2011 and in August 2011. The paper is organized as follows: Section 2 describes field observations. Section 3 describes form and frictional drag formulations. Estimates of form drags and roughness length scales are provided in sections 4 and 5, respectively. Discussion is given in section 6. A summary with major findings is in section 7. Last, a sensitivity study of the estimated form drag based on numerical simulations is provided in the appendix.

2. Observations

Sampling was conducted at the EFGB, located approximately 190 km southeast of Galveston, Texas, in the northwestern Gulf of Mexico (GoM). The EFGB is part of the National Marine Sanctuary System and is one of many banks formed by salt domes on the continental shelf. The EFGB is a biologically diverse coral reef consisting of brightly colored sponges, plants, and other marine life. The habitat map and an example of the size of a typical coral head are shown in Fig. 1. The EFGB is a pear-shaped bathymetric feature rising from below 100-m water depth to 18 m below the surface (Figs. 1, 2). The bank is about 10 km long and about 6 km wide, and its projected area to the horizontal plane encompassed by the 100-m bathymetry contour is approximately 40 km^2. The EFGB has steep lateral slopes (~50-m height change within 500-m distance) at the eastern and southern boundaries. The top, located just off the southern peak, is nearly flat with more gentle slopes westward and northward, but contains rough bathymetric elements such as corals (Figs. 1, 2). The top of the bank is dominated by

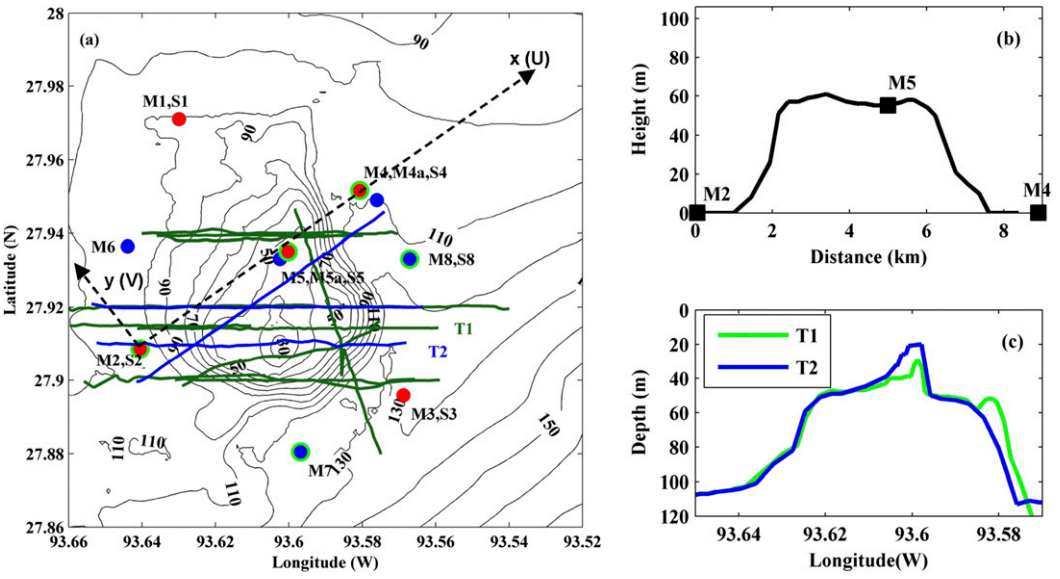

FIG. 2. (a) Bathymetric map of the bank with contours every 10 m. The red bullets are the long-term Barny mooring locations, and the blue bullets are the short-term mooring locations. The locations of Ppods are marked in green circles. Note that the string moorings (S1–S5 and S8) were located about 100–200 m from the Barny locations. The green lines are June transects, and blue lines are August transects. The black dashed lines shows the coordinate system (x, y), where the x axis is parallel to the M2–M5 mooring line, and the y axis is perpendicular to the mooring line. Note that U is positive in the x direction, and V is positive in the y direction. (b) Cross section of bathymetry along M2–M5–M4 line. Distance (positive eastward) is from M2 and the height of bank (positive upward) is from 106-m bathymetry contour. (c) Longitude–depth cross sections of bathymetry along T1 and T2 transects.

relatively large, head-forming corals, with *Montastrea annularis*, known as boulder star corals, composing 30% of the total coverage between 18- and 36-m depth, and the species *Diploria strigosa, Colpophyllia natans, Montastrea cavernosa, Millepora alcicornis*, and *Porites astreoides* account for an additional 20% coverage (Fig. 1). The total coral coverage on the upper reef averages approximately 55% (Bright et al. 1984). Between 30- and 40-m depth, algal ridges are common, and below 50-m, algal nodules (rhodoliths) are dominant. In these deeper zones nodules can reach 1–2-m height due to lower current velocities (Minnery 1990; Fig. 1).

The observational program over the EFGB consisted of two 6-month mooring deployments (from December 2010 to June 2011 and from June 2011 to December 2011), a 2-week intensive observational period (IOP) from 31 May to 14 June 2011, and a week-long microstructure survey during a coral spawning event in August 2011 as a part of the MORT and COB projects. Two ships [Research Vessel (R/V) *Pelican* and R/V *Manta*] took measurements over the bank during the IOP. Microstructure surveys were conducted from the R/V *Manta*, while moorings were deployed from the R/V *Pelican*. Detailed discussions of instrumentation, data collection, sampling methods, and data processing for the long-term and short-term deployments are in Teague et al. (2013) and in Jarosz et al. (2014, manuscript submitted to *J. Geophys. Res.*). Here we describe the subset of the data relevant to this study, that is, measurements made during the IOP and in August 2011 as well as from the moorings deployed during the second half of the COB experiment (June–December 2011). Bathymetry and locations of these short- and long-term moorings at the EFGB are shown in Figs. 1a and 2a.

a. Moorings: Currents, pressure, and hydrography

A total of 10 Teledyne RD Instruments' (RDI) acoustic Doppler current profilers (ADCPs) were deployed in bottom-mounted, trawl-resistant housings referred to as "Barnys" (Perkins et al. 2000) at stations M1–M8, measuring east, north, and vertical velocities (Figs. 1, 2a). The ADCP at M5 operated at 600 kHz and all others operated at 300 kHz. Transducer heads were approximately 0.5 m above the sea floor. Yearlong currents and hydrographic fields were collected from five ADCP moorings (M1–M5) and four subsurface string moorings (S1–S4) equipped with temperature T, conductivity C, and pressure P (TCP) sensors. ADCPs recorded nearly full water column current profiles every 15 min (an ensemble average of 120 realizations) during long-term deployments. During the IOP high temporal resolution, current and hydrographic data were collected

from another five bottom-mounted ADCPs at stations M4a, M5a, M6, M7, and M8 and two string moorings at S5 and S8. Samples were averaged every minute at M4a, M5a, and M6 and every 2 min at M7 and M8. Vertical bin sizes were 1 m at M5a, 2 m at M4a, and 4 m at M6, M7, and M8. Accuracy for the ADCP measurements is 0.5% of the observed water velocity $\pm$ 0.5 cm s^{-1}.

Barny moorings were also equipped with Ppods (Moum and Nash 2008). Ppods are modified Paroscientfic pressure sensors and have a precision of about 0.14 mm or 1 Pa (1 Pa = 1 N m^{-2}). A total of five Ppods were deployed during MORT (Fig. 2a) at M2, M4, M5, M7, and M8, and their pressure is referred to as P_{M2}, P_{M4}, P_{M5}, P_{M7}, and P_{M8}. Three of the Ppods (P_{M2}, P_{M4}, and P_{M5}) were deployed along a line over the bank for a period of nearly 6 months (between June and December 2011), and the other two (P_{M7} and P_{M8}) were deployed for 2 weeks in June 2011 during the IOP. We noted mismatches in time stamps and nonuniform sampling rates in the long-term deployed Ppods. The first step was to obtain correct time stamps and sampling rates. The time stamps of P_{M2} and P_{M4} were accurate, but their sampling rates deviated from 1 Hz, indicating drifts in the sampling clocks. Note that the average sampling rate was 0.97 Hz. To fix sampling rates caused by clock drifts, we resampled (i.e., interpolated) P_{M2} and P_{M4} data at 1-Hz sampling rates between accurate time stamps of starting and ending times. We noted that the accurate clock in P_{M5} was broken in August 2011, but the sampling clock had an accurate time stamp with a sampling rate of 1 Hz; when compared with the rest of the Ppods, the sampling clock in P_{M5} was consistent with the other accurate clocks in P_{M2} and P_{M4}. Therefore, we used the time stamp of the sampling clock as the accurate time stamp for P_{M5}.

Four TCP string moorings (S1–S4) were deployed close to M1–M4 during the first half of the deployment and only three (S2–S4) were redeployed near M2–M4 during the second half (Fig. 2a). Each string mooring contained 8 to 12 TCP sensors that were approximately equally spaced between 7 and 12 m below the surface and 1 m above the bottom (Teague et al. 2013). We do not address processing and data quality issues here, since those topics were discussed in Teague et al. (2013).

For the current data, we used local coordinates with the U component oriented toward the axis of the M2–M4 mooring line and the V component oriented perpendicular to the mooring line (Fig. 2). We rotated ADCP currents by 19° counterclockwise to the horizontal direction to match with the direction of the form drag estimated in section 4. Low-frequency east–west flow showed a two-layer structure around the bank (Teague et al. 2013). A similar flow pattern was found in U. Figure 3 shows the depth-averaged low-frequency [<0.02 cycles per hour (cph)] currents (U_U, V_U) in the upper 50-m layer. The flow U_U was nearly eastward during the first half of the record and changed direction after yearday 263 (Figs. 3a,b). Currents in the lower layer (U_L, V_L) were smaller than in the upper layer and were highly influenced by the bank (Figs. 3c,d; Teague et al. 2013). Mean currents approximately 20 m above the bottom followed the bottom topography (Teague et al. 2013). Shipboard and moored velocity measurements made during the IOP (2–13 June 2011) showed generation of submesoscale and mesoscale motions and reversals of bottom currents on the lee side of the bank (Jarosz et al. 2014, manuscript submitted to *J. Geophys. Res.*). Based on all the ADCP velocity records, we noted that the currents in the upper 50-m layer at M1 were least affected by the bank. M1 was located at the northwest corner of the bank where the bottom slope was less steep compared to slopes south and east side of the bank (Fig. 2). Near-surface intensified high-frequency currents (>0.2 cph) were observed over the top of the bank and were closely related with wind and surface waves (Wijesekera et al. 2013).

The spectra of U_U and V_U show several distinctive frequency bands associated with tidal/inertial waves and subtidal flows (Fig. 4). The near-inertial period (25.52 h) lies between the K_1 (23.93 h) and O_1 (25. 82 h) tidal periods. Teague et al. (2013) reported that near-inertial currents were as large as 20 cm s^{-1}, especially during summer months, and that barotropic diurnal tides were less than about 4 cm s^{-1}. The tidal–inertial components of east–west and north–south directions had similar magnitudes, while the semidiurnal components in the north–south direction were stronger than the east–west components (Fig. 4). The subtidal band contains 4–6-, 10–12-, and 16–17-day fluctuations. There was no clear spring–neap tidal signal (period ~14 day) in the subtidal band (Fig. 4). In the northern GoM, the 4–6-day signal may relate to synoptic-scale weather systems (e.g., Donohue et al. 2006). Donohue et al. (2006, 2008) observed 16- and 14-day oscillations in bottom pressure in the north central GoM, but these signals were unexplained. However, Donohue et al. (2008) further noted that the 16-day signal is in phase with water level variations measured by coastal tide gauges on the west Florida shelf.

Near-surface temperature showed seasonal warming in summer and cooling in late fall (Fig. 3e). The advection of cold water, especially near the bottom, appeared after yearday 240 [lasting close to the end of the observational period (Fig. 3e)] and changed the vertical structure of temperature and density fields, which in turn

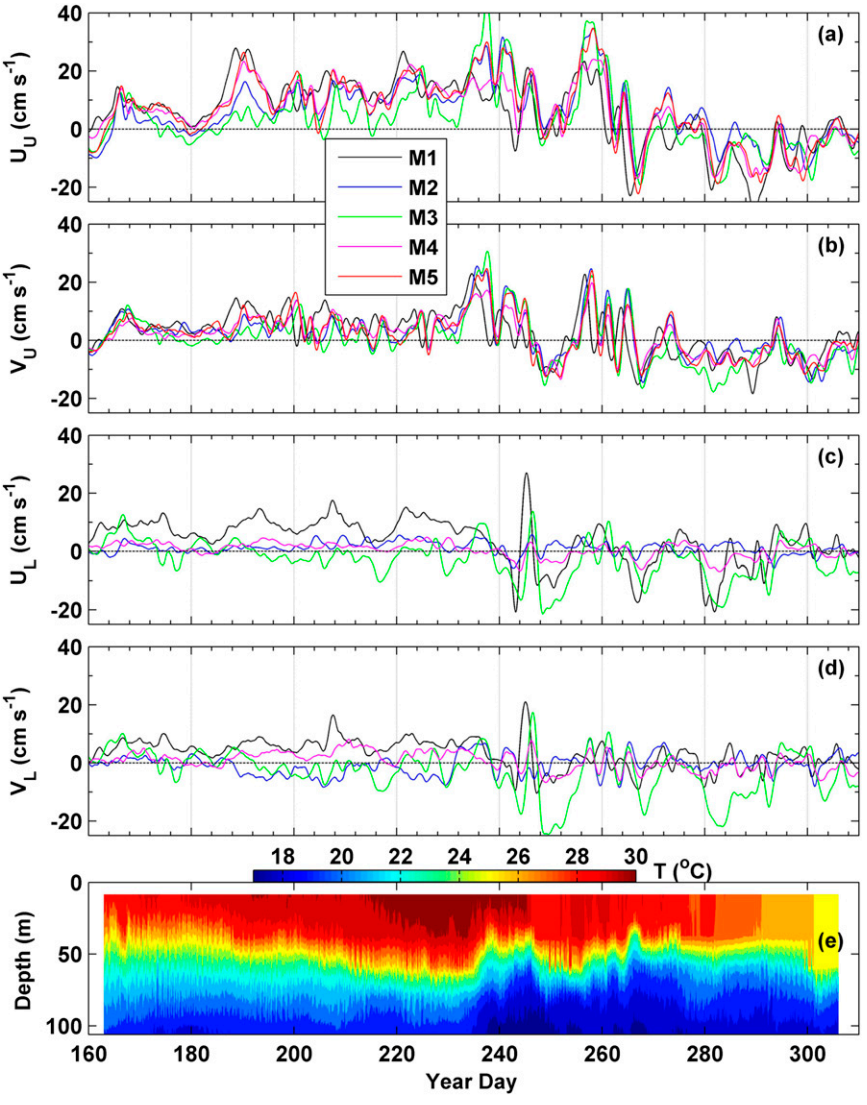

FIG. 3. Time series of 48-h low-pass filtered upper-layer (above 50 m) and lower-layer (below 50 m) velocities (cm s^{-1}). (a) Upper-layer velocity along the direction of the mooring axis M2–M4 (U_U). (b) Upper-layer velocity perpendicular to the mooring axis (V_U). (c) Lower-layer velocity along the direction of mooring axis M2–M4 (U_L). (d) Lower-layer velocity perpendicular to the mooring axis (V_L). (e) Color image of depth–time series of 15-min averaged temperature (°C) at S2.

altered bottom pressure across the bank on subseasonal to seasonal time scales. Teague et al. (2013) suggested a plausibility of advection of cold water by eddies in the region. In the following analysis, we focus on motions that can be well resolved by our data, and therefore we limit the computation of the form drag to tidal (12–25 h) and subtidal (4–17 days) motions.

b. *Ship surveys: Currents, hydrography, and microstructure*

Ship surveys were conducted from the National Oceanic and Atmospheric Administration (NOAA) R/V *Manta*, a 25-m catamaran vessel out of Galveston, Texas. A 300-kHz RDI ADCP was mounted on the side of the boat and recorded currents with a vertical bin size of 4 m. Velocities were processed using the University of Hawai'i's Common Oceanographic Data Access System (CODAS; Firing et al. 1995) to correct for ship motion and were averaged over 4-min intervals. A BioSonics DT-X digital scientific echosounder was used to acquire bathymetric data based on acoustic backscatter. The echosounder sampled at a rate of 3 Hz with a frequency of 123 Hz. The average horizontal sampling distance was approximately 25 cm.

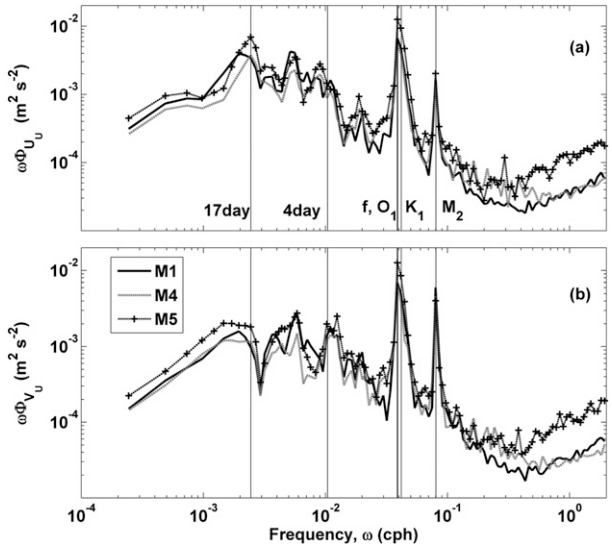

FIG. 4. Depth-averaged frequency-weighted velocity spectra in the upper 50 m based on time series of velocity shown in Figs. 3a and 3b. (a) U_U and (b) V_U. Spectra at M1, M4, and M5 are plotted. The vertical lines denote frequencies of M_2, K_1, O_1, f (inertial), 4-day, and 17-day motions.

Additionally, vertical profiles of small-scale velocity and temperature along with finescale T, C, and P fields were collected from a free-falling Rockland Scientific vertical microstructure profiler (VMP), equipped with a pressure sensor, shear probes, a fast thermistor, microconductivity, and Sea-Bird Electronics temperature and conductivity sensors (e.g., Wolk et al. 2002). These profiles were collected while the R/V *Manta* was drifting or steaming slowly along quasi-straight lines over the bank at speeds of 0.5 to 1 m s^{-1} (blue and green lines in Fig. 2a). The velocity shear accuracy was 5%, and the VMP probe had an average descent speed of 0.8 m s^{-1}, producing shear measurements approximately every 0.2 cm. Shear measurements were utilized to estimate turbulent kinetic energy (TKE) dissipation rates using $\varepsilon = 7.5\nu\overline{(\partial u/\partial z)^2}$, where ν is the kinematic viscosity of water estimated from concurrent temperature observations, and $\partial u/\partial z$ is the velocity shear (Gregg 1987). The velocity shear variance was calculated by integrating the spectrum for the wavenumber range from 2 to 30 cycles per meter (cpm), while the spectrum was estimated in bins of 1024 shear data records, with a 512 record overlap. We noted that more than 90% of the spectral variance was between 2 and 30 cpm wavenumbers. In this study, we focus on the dissipation estimates near the bottom. A detailed discussion of dissipation estimates and their distribution during the IOP is given in Jarosz et al. (2014, manuscript submitted to *J. Geophys. Res.*).

3. Form and frictional drags

a. Form drag

The form drag is defined as the spatial integral of the product of the bottom pressure anomaly and the lateral slope of the bathymetry (e.g., Gill 1982, p. 145; Baines 1995). The form drag along a line of pressure measurements is (e.g., McCabe et al. 2006; Warner et al. 2013)

$$D_{\text{form}}(t). = -\int_{x_1}^{x_2} p_b'(x,y,t)h_x\,dx \quad [\text{N m}^{-1}], \qquad (1)$$

where p_b' is the bottom pressure anomaly in N m^{-2}, h is the bottom height in meters, h_x is the lateral gradient of the bank in the direction where the drag is estimated, t is the time, x and y are the orthogonal coordinates over the bank, and x_1 and x_2 are points of the equal depth on either side of bank (Fig. 2). The power (P_{form}) associated with D_{form}, or the rate of energy loss of the background flow due to the form drag, is defined as the product of D_{form} and the free-stream velocity undisturbed by the topographic feature U_m (Gill 1982, section 8.7; Warner et al. 2013), where

$$P_{\text{form}} = D_{\text{form}}U_m. \qquad (2)$$

The drag coefficient C_{DF} associated with the form drag [(1)] is defined as (e.g., Lott and Miller 1997; Vosper et al. 1999; Warner and MacCready 2009)

$$C_{\text{DF}} = \frac{D_{\text{form}}/h_0}{-0.5\rho_0|U_m|U_m}, \qquad (3)$$

where ρ_0 is the seawater density, and h_0 is the topographic height. Here a minus sign is included since the drag and the velocity have opposite signs. The term C_{DF} is an $O(1)$ quantity and is referred to as the bluff–body drag coefficient (Warner et al. 2013). The quantity C_{DF} is widely used in engineering applications. To give an oceanographic context, we also defined a bulk (form) drag coefficient C_D, associated with D_{form} as an equivalent frictional drag coefficient based on mean flow velocity U_m (e.g., Warner et al. 2013), where

$$C_D = \frac{D_{\text{form}}/l_0}{-0.5\rho_0|U_m|U_m}, \qquad (4)$$

and l_0 is the topographic length. Equation (4) defines the bulk drag coefficient in the same way as the frictional drag coefficient, although the near-bottom velocity is typically used in computing the frictional drag resulting from bottom roughness elements [see (13)]. The form drag coefficient C_D can be treated as an enhanced frictional drag coefficient from a numerical modeling perspective. From (3) and (4), $C_{\text{DF}}/C_D = l_0/h_0$, and for

the EFGB (Fig. 2) with $h_0 \sim 50\,\mathrm{m}$, and $l_0 \sim 9\,\mathrm{km}$, $C_{DF}/C_D \sim 180$.

The first step in estimating the form drag is to determine p_b' from bottom pressure measurements. The bottom pressure sensors, deployed during MORT, measured the total pressure at the seafloor p_b, which includes atmospheric pressure, pressure resulting from surface elevation and water density, and nonhydrostatic pressure. Following Moum and Smyth (2006) and Warner et al. (2013), we express the total pressure $p(X, t)$ at depth z by integrating the vertical momentum balance from z to the sea surface height $\eta(x, y, t)$:

$$p(X,t) = p_{\mathrm{Atm}} + g\rho_0[\eta(x,y,t) - z] + g\int_z^\eta \overline{\rho}(z',t)\,dz' + g\int_z^\eta \rho'(X,t)\,dz' + \rho_0\int_z^\eta Dw/Dt\,dz', \tag{5}$$

where $p(X, t)$ varies in all directions; $X = (x, y, z)$ represents a right-handed coordinate system with the x axis parallel to the bottom pressure sensor array, the y axis perpendicular to the sensor array, the z axis positive upward, and $z = 0$ at the bottom; p_{Atm} is the atmospheric pressure at the surface and is assumed to be uniform over the domain; D/Dt is the material derivative; w is the vertical velocity; and g is the gravitational acceleration ($9.81\,\mathrm{m\,s^{-2}}$). The density is expressed as $\rho(X, t) = \rho_0 + \overline{\rho}(z, t) + \rho'(X, t)$, where ρ_0 = constant, $\overline{\rho}(z, t)$ is the background stratification, and $\rho'(X, t)$ is the density fluctuation. The sea surface can be divided into four components:

$$\eta(x,y,t) = \overline{\eta}(t) + \eta_{Tf}(x,y,t) + \eta_{Ti}(x,y,t) + \eta'(x,y,t), \tag{6}$$

where $\overline{\eta}(t)$ is the spatially averaged sea surface height; $\eta_{Tf}(x, y, t)$ is the contribution to sea surface height associated with the sea surface slope resulting from rotational effects. Here barotropic pressure gradients associated with surface elevation are balanced by the Coriolis force; $\eta_{Ti}(x, y, t)$ is the surface elevation resulting from accelerations/decelerations of flow over the bank, and $\eta'(x, y, t)$ is the remaining sea surface height anomaly (e.g., Warner et al. 2013). By combining (5) and (6) we obtain

$$p(X,t) = p_{\mathrm{Atm}} + g\rho_0\overline{\eta}(t) + g\rho_0\eta_{Tf}(x,y,t) + g\rho_0\eta_{Ti}(x,y,t) + g\rho_0\eta'(x,y,t) - g\rho_0 z + g\int_z^\eta \overline{\rho}(z',t)\,dz + g\int_z^\eta \rho'(X,t)\,dz' + \rho_0\int_z^\eta Dw/Dt\,dz'. \tag{7}$$

Pressure terms, which vary in the x direction, contribute to the form drag given in (1). The pressure anomaly that is dynamically relevant to the flow over the bank is given by

$$p'(X,t) = g\rho_0\eta_{Ti}(x,y,t) + g\rho_0\eta'(x,y,t) + g\int_z^\eta \rho'(X,t)\,dz' + \rho_0\int_z^\eta Dw/Dt\,dz'. \tag{8}$$

Rotational contributions to sea surface height are excluded because their associated velocity component is orthogonal to the direction of the form drag.

b. *Frictional drag*

Frictional stress resulting from turbulence and viscous effects (Schlichting 1962; Tennekes and Lumley 1972) is

$$F_m = \rho\langle uw\rangle - \rho\nu\frac{\partial\tilde{U}}{\partial z} \quad [\mathrm{N\,m^{-2}}], \tag{9}$$

where $\tilde{U}$ is the mean lateral velocity, u and w are the lateral and vertical velocity fluctuations, ν is the kinematic viscosity, and z is the distance from the sea floor (positive upward) as defined above. The angle brackets denote the average over turbulent motions. In the presence of strong surface waves, the turbulent bottom stress $-\rho\langle uw\rangle$ over the continental shelf and shallow banks may include a stress component from surface wave–induced oscillatory currents (e.g., Grant and Madsen 1982). The surface wave–driven stress is significantly larger over the shelf during severe storms (e.g., Wijesekera et al. 2010), but in the following analysis, we limit our bottom drag computations to mean currents, since hurricane strength winds were not present over the EFGB during the observational period. As discussed below, we estimated bottom roughness lengths and frictional drag coefficients when microstructure observations were available for 10 days in June and August 2011. Winds were less than $6\,\mathrm{m\,s^{-1}}$ and surface wave heights were 0.2–0.5 m (Wijesekera et al. 2013). Surface wave–induced bottom currents were negligible over the top of the bank. Therefore, the surface wave–induced bottom frictional effects or "the apparent roughness lengths" were not a significant factor. The wall boundary layer theory provides an estimate of the roughness length of bottom roughness elements.

Sufficiently far from the boundary $z \gg \nu/u$ or at sufficiently large Reynolds numbers $uz/\nu \gg 1$, a layer (referred as the inertial layer) exists in which the overall dynamics of turbulence is independent of viscosity. In this layer, $F_m = \rho\langle uw\rangle = -\tau$, where τ is the bottom stress. The flux term can be rewritten as a downgradient flux, $F_m = -\rho K_m \partial\tilde{U}/\partial z$, where K_m is the turbulent transfer coefficient having dimensions of velocity and length and $\partial\tilde{U}/\partial z$ is the vertical gradient of the mean flow. For the inertial layer, $K_m = \kappa u_* z$, $|\tau| = \rho u_*^2$, and

$$\frac{\partial\tilde{U}}{\partial z} = \frac{u_*}{\kappa z}, \tag{10}$$

where κ is von Kármán's constant (0.41), and u_* is the water friction velocity that is independent of z. The turbulent fluxes in the inertial layer are nearly independent (within 10%–20%) of the distance from the boundary. By integrating (10), we can obtain a mean velocity profile:

$$\tilde{U} = \frac{u_*}{\kappa}\log\left(\frac{z}{z_0}\right), \tag{11}$$

where z_0 is the roughness length and is determined by the geometry of the surface. The term z_0 is a small fraction of the frictional element heights; for example, for closely packed sand grains of size λ, $z_0 = \lambda/30$ (Nikuradse 1950).

Suppose we have observations in the inertial layer at $z = z_a$, where $\tilde{U}(z_a) = \tilde{U}_a$, then squaring (11), we solve for the magnitude of the bottom stress:

$$|\tau| = \rho[\kappa^2 \log(z_a/z_0)^{-2}]\tilde{U}_a^2 = \rho C_d \tilde{U}_a^2, \tag{12}$$

where

$$C_d = [\kappa/\log(z_a/z_0)]^2 \tag{13}$$

is the frictional drag coefficient. Within the inertial layer the production of TKE by sheared currents approximately balances the dissipation rate, and thus

$$u_* = (\varepsilon\kappa z)^{1/3}, \tag{14}$$

where ε is the TKE dissipation rate (e.g., Dewey and Crawford 1988). The roughness length becomes

$$z_0 = z_a \exp(-\kappa\tilde{U}_a/u_*). \tag{15}$$

In the following, we use velocity and TKE dissipation rate profiles to compute the roughness length and the associated frictional drag coefficient over the EFGB.

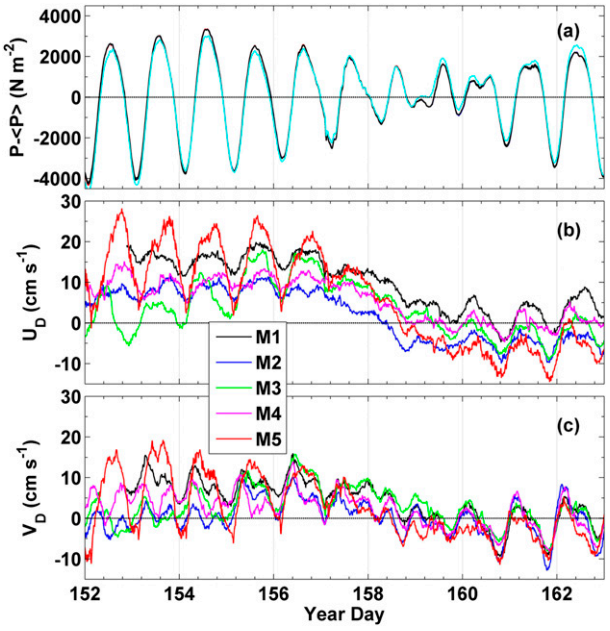

FIG. 5. (a) Demeaned bottom pressure ($P - \langle P\rangle$) at M2, M4, M5, M7, and M8 between 2 Jun (yearday 152) and 13 Jun (yearday 163) 2011, where $\langle P\rangle$ is the time-averaged pressure. Pressure at M7 (south of the bank; Fig. 2a), marked in cyan differs from the rest of the observations. (b) Depth-averaged velocity in the direction of the mooring axis (U_D) and (c) velocity perpendicular to the mooring axis (V_D) at M1–M5.

4. Evaluation of form drag

a. Bottom pressure anomaly from Ppods

Figure 5 shows bottom pressure fluctuations at five mooring sites (Figs. 1, 2) between 2 June (yearday 152) and 13 June (yearday 163) 2011. The pressure fluctuations were constructed by removing the temporal mean for a given record length of 12 days. The demeaned pressure fluctuations show diurnal tides and a segment of the spring–neap cycle. Tides around and over the bank had similar phases (Fig. 5a) since the spatial scales of tidal motions are much larger than the lateral spacings between moorings. Unlike pressure, the depth-averaged velocities at M1–M5 were not always in phase, especially at the beginning of the records (Figs. 5b,c). While pressure fluctuations were dominated by diurnal tides, velocity fluctuations contained combinations of tides and near-inertial waves.

Pressure spectra calculated at M2, M4, and M5 (Fig. 6) show several distinctive features including the surface–gravity wave band between 0.08 and 0.2 Hz, the infragravity wave band between 0.002 and 0.08 Hz, the semidiurnal M_2 tide (period = 12.42 h), and the diurnal tidal bands K_1 (period = 23.93 h) and O_1 (period = 25.82 h). Our pressure spectra also indicate variability in the synoptic time

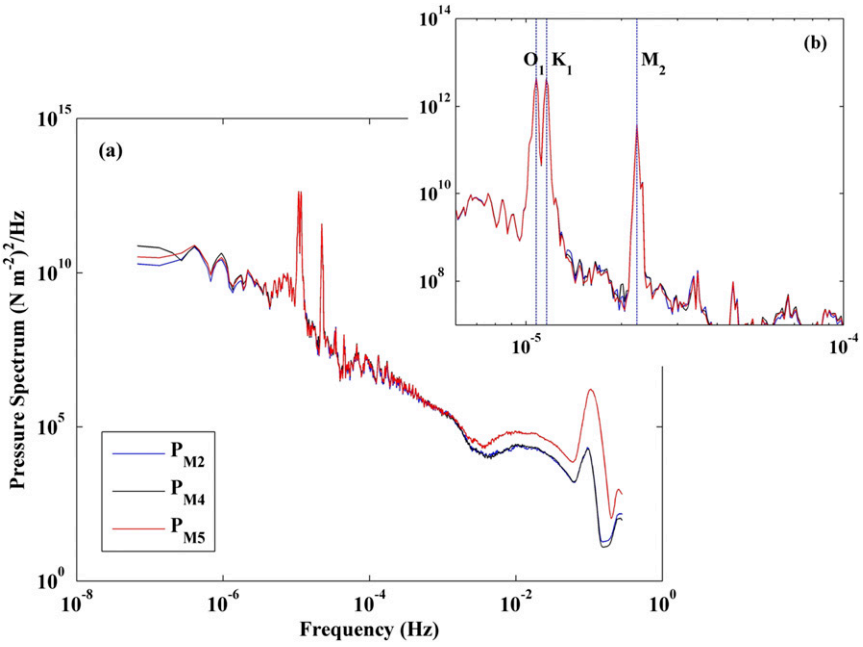

FIG. 6. (a) Frequency spectra of bottom pressure at M2, M4, and M5. The spectra were based on the entire pressure record with a sampling rate of 1 Hz. Spectra were averaged into 2^{10} frequency bins. (b) Enlarged plot showing diurnal tides O_1 and K_1 and semidiurnal tide M_2.

scale (4–6 days) and in 10–17-day fluctuations, similar to velocity spectra shown in Fig. 4. The amplitude of a given tidal frequency was estimated by integrating the pressure spectrum for a specified spectral band, and the amplitudes of O_1, K_1, and M_2 tides are 0.17, 0.17, and 0.06 m, respectively. The pressure spectrum (Fig. 6) has a slope of about -1.5 between 10^{-4} and 10^{-3} Hz. Teague et al. (2013) examined velocity components of tides and near-inertial waves (period = 25.52 h). They reported that tidal velocities were smaller than near-inertial velocities, and magnitudes of K_1 and O_1 were about 3–5 cm s^{-1}. The magnitude of the M_2 tidal velocity was about 2.5 cm s^{-1}.

We adopted the following procedure to compute pressure anomalies. First high-frequency pressure fluctuations and spikes were removed by filtering raw pressure to remove frequencies higher than 10^{-3} Hz. Second, seasonal and subseasonal motions with time scales greater than 30 days were filtered out, since these motions are not well resolved, and our focus is on tidal and subtidal (4–17 day) oscillations. These bandpass-filtered pressure fluctuations at M2, M4, and M5 are referred as $\tilde{P}_{M2}$, $\tilde{P}_{M4}$, and $\tilde{P}_{M5}$. The 30-day high-pass filter basically removed the largest term ($\rho_0 gz$) in (7). The sea surface elevation $\rho_0 g\overline{\eta}(t)$ was removed by subtracting the reference or the background pressure at a location away from the bank. Here we used $\tilde{P}_{M2}$ as the reference pressure record. This choice of the reference pressure does not affect the form drag calculation, and any Ppod pressure could have been used as a background. The value $\rho_0 g\overline{\eta}(t)$ is spatially uniform and therefore does not affect the form drag calculation. Pressure anomalies at M4 (ΔP_{M4}) and at M5 (ΔP_{M5}) were obtained by removing $\tilde{P}_{M2}$ from $\tilde{P}_{M4}$ and $\tilde{P}_{M5}$, where $\Delta P_{M4} = \tilde{P}_{M4} - \tilde{P}_{M2}$ and $\Delta P_{M5} = \tilde{P}_{M5} - \tilde{P}_{M2}$ (Fig. 7). Note the pressure anomaly at M2, where ΔP_{M2} became zero. The subtraction of the reference pressure also removed the atmospheric pressure p_{Atm}, since p_{Atm} was assumed to be uniform over the bank. The background stratification term $g\int_z^{\eta}\overline{\rho}(z', t)\,dz'$ was not computed because the time-dependent, depth-averaged density was not well known. Time–depth series of hydrographic data from three TCP moorings at S2, S3, and S4 were available, but lateral and vertical resolutions of the density field were very coarse to make an accurate estimate of the background stratification term. This term is spatially uniform, and therefore the subtraction of the reference pressure $\tilde{P}_{M2}$ removes the term $g\int_z^{\eta}\overline{\rho}(z', t)\,dz'$ from pressure anomalies at M4 and M5. The sea surface tilt due to rotational effects was estimated from the geostrophic balance $g\partial\eta_{Tf}/\partial x = f\overline{V}$, where $\overline{V}$ is the low-pass filtered (periods greater than 48 h), depth-averaged velocity perpendicular to the mooring line, and f is the Coriolis parameter. We noted that $\overline{V}$ was nearly uniform around the bank (not shown). Therefore, the pressure induced by the sea surface height due to rotational effects at a given location along the mooring line was approximated from $g\rho_0\eta_{Tf} \approx \rho_0 f\overline{V}(x - x_{M2})$. For $f = 6.84 \times 10^{-5}$ s^{-1},

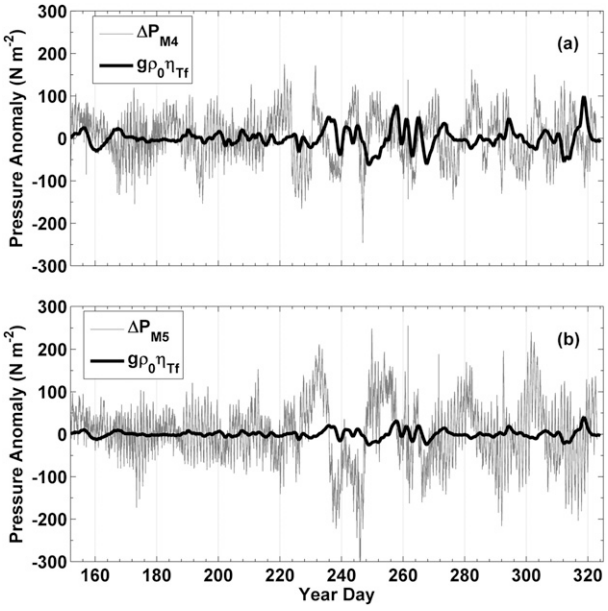

FIG. 7. Bottom pressure anomalies (thin gray lines) at (a) M4, $\Delta P_{M4} = \tilde{P}_{M4} - \tilde{P}_{M2}$, and (b) M5, $\Delta P_{M5} = \tilde{P}_{M5} - \tilde{P}_{M2}$. Barotropic pressure anomaly estimated from rotational effects, $g\rho_0\eta_{Tf} \approx \rho_0 f\overline{V}(x - x_{M2})$, are marked by thick black lines.

$\overline{V} = 0.1\,\mathrm{m\,s^{-1}}$, $\rho_0 = 1000\,\mathrm{kg\,m^{-3}}$, and $x = x_{M4}$ with $(x_{M4} - x_{M2}) = 9\,\mathrm{km}$, the resulting pressure anomaly at M4 is as large as $100\,\mathrm{N\,m^{-2}}$ (Fig. 7a).

As described above, the bottom pressure anomalies west, east, and in the middle of the bank (M2, M4, and M5, respectively) were obtained by (i) bandpass filtering of pressure between 1000 s and 30 days, (ii) subtracting a selected reference pressure outside the bank (i.e., pressure at M2), and (iii) subtracting the pressure due to rotational effects. Bottom pressure anomalies at M2, M4, and M5 are, respectively, $p'_{bM2} = 0$, $p'_{bM4} = \Delta P_{M4} - \rho_0 f\overline{V}(x_{M4} - x_{M2})$, and $p'_{bM5} = \Delta P_{M5} - \rho_0 f\overline{V}\,(x_{M5} - x_{M2})$. The bottom pressure anomalies were dominated by the combined external, internal, and inertial pressure anomalies (ΔP_{M4} and ΔP_{M5}). The rotational effect that depends on the relative distance from M2 is important, especially at M4, but it is a smaller term at M5 (Fig. 7). Bottom pressure fluctuations (Fig. 7) show multiple timescale variability in ΔP_{M4} and ΔP_{M5}. They were about 50–$100\,\mathrm{N\,m^{-2}}$ at tidal frequencies and about 50–$200\,\mathrm{N\,m^{-2}}$ for low-frequency motions (periods ~ 4–17 days).

b. Form drag

We used three pressure sensors at M2, M5, and M4 (Fig. 2a) to compute the form drag over the bank. The drag was computed along the mooring line that was oriented about 19° counterclockwise from the east–west direction (Fig. 2). The topographic section along the mooring line is close to ''top hat''–shaped bathymetry. In general, the EFGB has steeper slopes along the east and south boundaries and a significant portion of the bank top is relatively flat, except near the peak (Fig. 2). The major challenge is to evaluate the form drag [(1)] from only three pressure measurements. Hafner and Smith (1985) estimated the form drag over the European Alps using a limited number of pressure measurements. They transformed the surface integral [(1)] to the flux integral and evaluated the form drag as the product of the horizontal, locally constant pressure gradient and the volume of the mountain terrain. This is the equivalent of assuming that the local pressure gradient is linear between two nearby observation sites. Hafner and Smith (1985) discussed the uncertainty of pressure that was determined by a linear formula based on their surface stations.

The form drag is large in regions where both bathymetric slopes and pressure anomalies are significant. Warner et al. (2013) examined the sensitivity of a number of pressure measurements by evaluating the integral [(1)] over a sloping headland, TTP in Puget Sound, Washington, and found that four sensors (two on either slope of the ridge; Fig. A1) can provide an accurate estimate. We also examined sensitivity for our three-point measurement setup (one on the top and one on either side of the ridge; Fig. A1) using Warner's (2012) numerically generated pressure fields over the TTP ridge. As described by Warner (2012), at TTP, the large bottom pressure anomalies were found where the topography was the steep. The model was able to capture some, but not all of these pressure anomalies. The spatial resolution of the model and the required smoothing of the topography for the model to run were major factors for simulating an accurate pressure field over the bank (Warner 2012). Since the Ppods in MORT were not located on the sloping sections of the topography, some of the largest pressure anomalies could have been missed.

A sensitivity analysis described in the appendix allows the examination of uncertainties in our computation based on three pressure measurements, although the geometrical and dynamical settings of this study and Warner et al.'s (2013) are not identical and the model results may not perfectly capture the distribution of bottom pressure anomalies due to numerical limitations. We compared form drag estimates based on multiple pressure measurements versus three pressure measurements as described in the appendix. We used three methods to compute the form drag over the bank. Method I computes the form drag by approximating bottom pressure for a given slope as the mean pressure between the top and the outer edge of the ridge and then multiplying it by the mean slope. Method II computes the form drag as a product of the observed slope and a linearly interpolated pressure between the outer edges

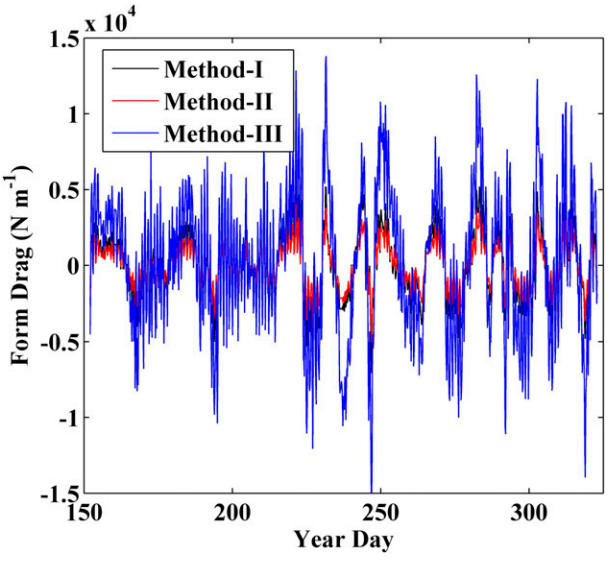

FIG. 8. Form drag estimated from the three methods described in the appendix.

and the top of the ridge. Method III computes the form drag as a product of the mean pressure for a given slope and the maximum magnitude of that slope. The estimates from methods I and II were comparable, but their maximum magnitudes were a factor of 2 smaller than those obtained from the method III and the fully resolved solution. Here we applied all three methods to compute the form drag along the M2–M4 mooring line, and results are illustrated in Fig. 8. Topographic gradients of the bank are small or near zero over the top and outside the 100-m bathymetry contour compared to the two major slopes of the bank (Figs. 1a, 2). Therefore, we can expect major contributions to the form drag from sloping boundaries. The EFGB is asymmetric, especially toward the southern end, where the lateral slopes over the bank are not negligible. We may not compute the form drag completely since our computation is limited to the east–west direction. Drags estimated from linearly interpolated pressure and from mean pressure are comparable. The form drag estimated from method III is twice large as those that calculated from methods I and II, similar to the findings in the appendix, indicating the sensitivity to the slope.

In the following analyses, we used the form drag computed from method II, similar to Hafner and Smith (1985), even though we may underestimate the expected value by a factor of 2. To examine the time variability of the total form drag, we examine tidal and subtidal components (time scales greater than 2 days) separately. The corresponding drag estimates based on method II are shown in Figs. 9a and 9b. The tidal band contains diurnal and semidiurnal tides, and the subtidal band contains multiple time scales (4–17 days). Here it is assumed that form drag can be expressed as a linear summation of several components. However, this assumption may have limitations when the processes that generate form drag become highly nonlinear. Frequency spectra of D_{form} were also computed to examine multiple time-scale processes related to the total form drag (Fig. 10). The semidiurnal and diurnal tidal components, 4–6-day synoptic time-scale variability, and 10–17-day low-frequency variability are major contributors to the total form drag, similar to the velocity spectrum shown in Fig. 3. The most dominant components of D_{form} are the diurnal and 4–17-day band with drag magnitudes in excess of $2000\,\text{N}\,\text{m}^{-1}$ (Table 1; Figs. 9). Note that the mean form drag for the tidal band was computed by averaging maximum tidal magnitudes, and the mean for the 4–17-day band was computed by averaging maximum magnitudes in every 4-day time interval.

The total form drag [(1), (8)] may contain inertial pressure exerted by the oscillatory nature of the flow (e.g., Warner and MacCready 2009; Warner et al. 2013). Because of tidal acceleration, such as during slack tides, the barotropic pressure gradient (i.e., sea surface slope $\partial\eta_{Ti}/\partial x$) is in the direction of the tidal acceleration ($\partial\overline{U}/\partial t$), which in turn generates an ''inertial drag'' or an ''apparent form drag'' without flow separation. We noted that the tendency term ($\partial\overline{U}/\partial t$) of the depth-averaged velocity was nearly uniform over and around the bank (not shown). Therefore, the pressure due to acceleration of the oscillatory flow is approximated as $g\rho_0\eta_{Ti} \approx \rho_0\partial\overline{U}/\partial t(x - x_{\text{M2}})$, where $\overline{U}$ is the depth-averaged velocity along the M2–M4 line, and the corresponding inertial drags (D_{iner}) for tidal and subtidal bands are plotted in Fig. 9. For tidal motions, D_{iner} is a significant part of the total form drag (Fig. 9a), but for subtidal motions (Fig. 9b), D_{iner} is negligible.

c. *Power:* P_{form}

Both currents and the estimated form drag consist of nonstationary processes, and conventional Fourier cospectrum analysis does not provide information about power variations within data records. Therefore, the power per unit length P_{form} is estimated as a product of D_{form} and U_m [(2)], where U_m is the free-stream velocity in the direction of the form drag at an upstream location where the flow is undisturbed by the topographic feature. Unfortunately, our observations outside the bank were close to the walls of the bank. The flow below the height of the bank was impacted by the topography, and among those observations, the flow in the upper 50 m at M1 was the least affected. Therefore, we used the upper 50-m averaged velocity U_U at M1 as the undisturbed mean flow U_m. A time series of P_{form} for the subtidal band at M1–M5 is shown in Fig. 11. For most occasions,

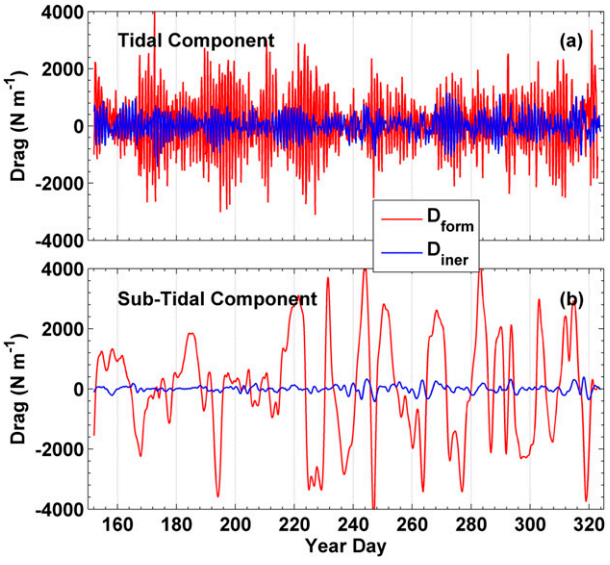

FIG. 9. Total form drag D_{form} based on interpolated pressure fluctuations (method II). (a) Tidal band and (b) subtidal bands (period > 2 days). The blue line in (a) and (b) is the inertial component of the form drag D_{iner} due to acceleration/deceleration of the flow.

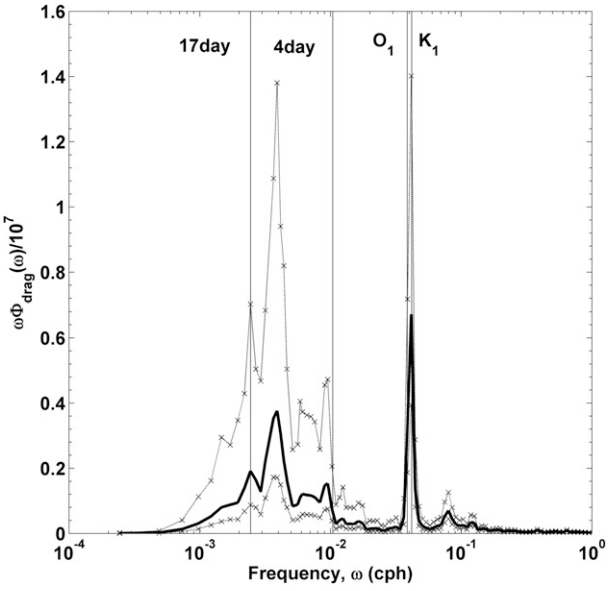

FIG. 10. Variance-preserving power spectra of the form drag $[(\text{N m}^{-1})^2 \times 10^{-7}]$. Thin lines with crosses denote 95% confidence limits. Vertical lines denote periods of K_1, O_1, 4-day, and 17-day motions.

$-U_U$ and D_{form} were in phase, indicating kinetic energy loss in mean currents due to the form drag over the bank with negative P_{form}. Positive values of P_{form} may reflect phase differences between the drag and the velocity, but some differences may be attributed to uncertainties in D_{form}. The energy loss ($P_{\text{form}} < 0$) has a wide range of variability with values as large as 800 W m^{-1} (Fig. 11). The 6-month averaged energy loss ($P_{\text{form}} < 0$) at M1 was about 85 W m^{-1} with 95% confidence limits between 76 and 93 W m^{-1} (Table 1). If the energy loss is computed from the depth-averaged velocity, the resulting 6-month averaged energy loss at M1 is 73 W m^{-1}, about 14% less than the estimate based on U_U (Table 1). The power associated with the diurnal tidal components was not computed, since tidal velocities were heavily contaminated by inertial motions. The magnitude of average energy loss per unit area, P_{form}/l_0, at subtidal (4 to 17 days) bands is about 10^{-2} W m^{-2}. Energy loss over the bank can be expressed as $(P_{\text{form}}/l_0)A_0$, where A_0 is the projection of the bank to the horizontal plane. The long-term average energy losses for the 4–17-day band is about 0.32 MW, where l_0 = 9 km, and A_0 (=40.76 km^2) is the projected bank area encompassed by the 100-m bathymetric contour.

d. Drag coefficient

The bluff–body drag coefficient C_{DF} [(3)] and the bulk drag coefficient C_D [(4)] were computed, and the estimates of C_D are presented here since $C_{\text{DF}}/C_D = l_0/h_0$. The bulk drag coefficient was calculated from the observed relation between $F_D(=-0.5\rho_0|U_m|U_m)$ and D_{form}/l_0 for the subtidal band, where U_m was set to U_U at M1 (Fig. 3a). The relationships between D_{form}/l_0 and F_D were explored for subtidal flows at all five mooring sites, and the bin-averaged D_{form}/l_0 is plotted as a function of F_D for U_U values at M1–M5 (Fig. 12). As discussed earlier, U_U at M1 is the best approximation for an undisturbed velocity for estimating C_D, but observations at M2–M5 also produced similar results. The slope of the scatterplots represents the bulk drag coefficient. The average C_D based on a least squares fit for $10 > F_D > -10$ is about 26×10^{-3}. Individual estimates of C_D (i.e., the ratio $D_{\text{form}}/l_0 F_D$) vary between 5×10^{-3} and 180×10^{-3} with a mean, standard deviation, and standard error of about 36×10^{-3}, 20×10^{-3}, and 5×10^{-3}, respectively. Here we excluded a few data points for $F_D < -10$ at M1. For the tidal band we used (4) to evaluate C_D from the tidal drag (Fig. 9; Table 1) and mean tidal currents from Teague et al. (2013; Table 1); C_D was not computed as a function of time because it is difficult to generate a time series of accurate tidal flow without contamination by inertial currents. The estimated bulk drag coefficients for the tidal and low-frequency bands are about (26–180) $\times 10^{-3}$ (Table 1).

e. Wave drag from linear theory

The approximation $D_{\text{form}}/l_0 \approx -0.5\rho_0 C_D|U_U|U_U$ (Fig. 12), especially at negative values of U_U, suggests that the

TABLE 1. Averaged form drag, velocity, power, and bulk drag coefficient [(4)]. Estimates of P_{form} were limited to low-frequency motions (Fig. 11). The magnitudes of K_1 and O_1 tidal velocities estimated by Teague et al. (2013) are also included in the table. The values inside the brackets are 95% confidence limits, and the values inside the curly brackets are minimum and maximum of the record. The term C_D for the diurnal tides was computed from velocity estimates given in Teague et al. (2013). The estimated bulk drag coefficient for semidiurnal tides by Warner et al. (2013) is given in the bottom row.

Variable	Diurnal tides (K_1 and O_1)	Subtidal: 4–17-day variability
D_{form} (N m^{-1}) (Fig. 9)	1500 [1400, 1600] {350, 4070}	2326 [1990, 2660] {352, 4550}
U_U (cm s^{-1})	7–11.4 [may contain inertial motions]	4.5–8.4
Tidal analysis (Teague et al. 2013)	3–5	—
P_{form} (W m^{-1}); $D_{\text{form}} \times U_U$ (upper-layer velocity, U_U at M1)	—	−85 [−93, −76]
$D_{\text{form}} \times \overline{U}$ (depth-averaged velocity; $\overline{U}$ at M1)	—	−73 [−77, −69]
Bulk drag coefficient [(4)]: C_D	180×10^{-3} {(150–220) $\times 10^{-3}$}	36×10^{-3} [(21, 51) $\times 10^{-3}$] {(5–180) $\times 10^{-3}$}
C_D from Fig. 12	—	26×10^{-3}
C_D (Warner et al. 2013)	Semidiurnal tides: 90×10^{-3}	—

form drag can be a linear function of flow speed as found by the linear theory of lee waves generated by bottom topography (e.g., Baines 1995). A formation of hydrostatic lee waves and the associated form drag for the nondimensional height of the bank, $h_n < 1$, and the nondimensional width, $a_n \gg 1$, have been studied extensively (e.g., Baines 1995). Queney (1948) calculated the wave drag (D_{wave}) of a mountain terrain profile ("Witch of Agnesi") with constant stratification and constant background velocity provided $h_n \ll 1$. In the following, we computed D_{wave} as a function of time using the observed velocity U_U and the background stratification N, where

$$D_{\text{wave}} = -\pi\rho_0 N h_0^2 U_U/8. \tag{16}$$

The minus sign in (16) is consistent with the definition of the form drag given in (1). The term N was estimated between depths of 15 and 65 m from density time series at S2, S3, and S4. The value h_0 was taken as the spatially averaged height of the bank above the 60-m bathymetry contour and is about 46 m (±5-m standard deviation). We could not calculate N at M1, so N at S2 was used. The bin-averaged D_{wave} is plotted as a function of D_{form} in

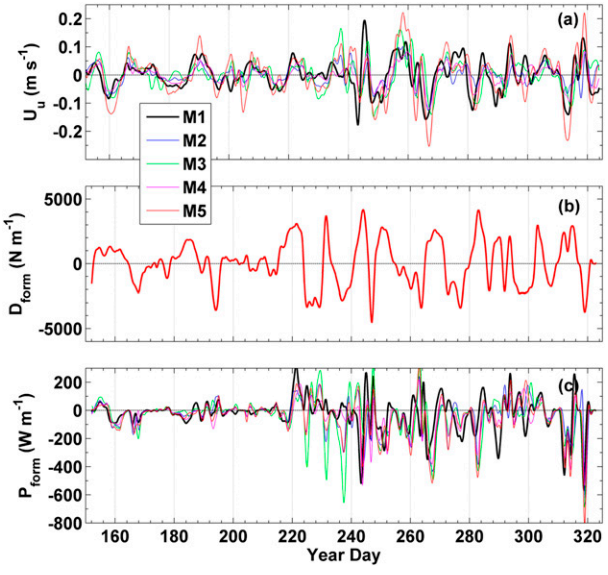

FIG. 11. Time series of (a) upper 50-m layer velocity U_U at M1–M5, (b) D_{form} for the subtidal band, and (c) P_{form} at M1–M5. Thick black lines in (a) and (c) are U_U and P_{form} at M1.

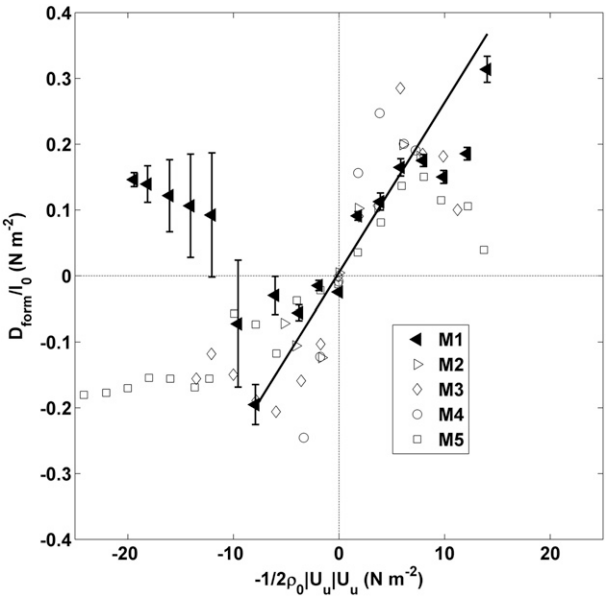

FIG. 12. Form drag per unit area D_{form}/l_0 for the subtidal band plotted against $F_D(=-0.5\rho_0|U_U|U_U)$ for velocities at M1–M5. The thick solid line denotes least squares fit for $F_D \geq -10$. The slope of the line represents the bulk drag coefficient (4) and is about 26×10^{-3}. The error bars (95% confidence levels) are plotted only for M1.

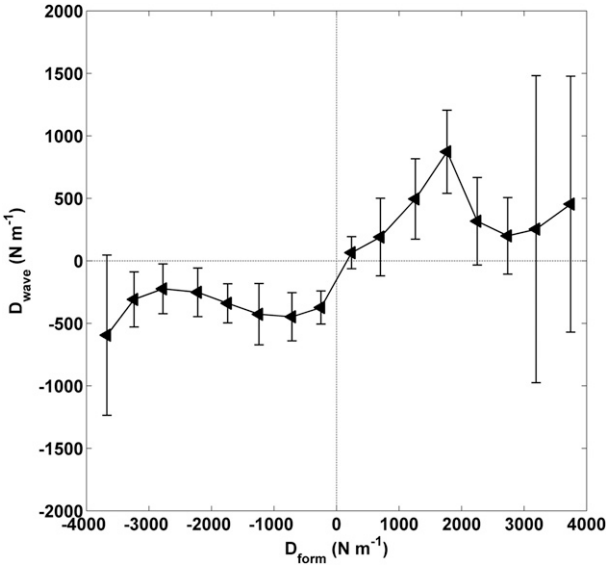

FIG. 13. D_{form} for subtidal motions vs the estimated wave drag from the linear theory [(16)] at M1 along with 95% confidence levels (vertical lines).

Fig. 13. Both D_{wave} and D_{form} have similar directions, but the averaged magnitudes of D_{wave} are smaller than D_{form}. This could be influenced by the terrain-shaped Witch of Agnesi used in (16), which is different from the three-dimensional pear-shaped EFGB. There was no apparent relationship between wave and form drags, especially for negative D_{form} (Fig. 13). The correlation between D_{wave} and D_{form} (Fig. 13) is less convincing compared to the quadratic drag approximation shown in Fig. 12. The observed parameter range reflects a blocking flow ($h_n \gg 1$), which is significantly different from Queney's nonblocked flow solution ($h_n \ll 1$). We discuss the applicability of linear theory in the discussion section.

5. Estimates of frictional drag

We compute the frictional drag coefficient C_d [(13)] and the roughness length z_0 [(15)] over the bank by combining measured TKE dissipation rates and currents near the bottom. The spacing between VMP profiles is approximately 200 m on average, much larger than individual coral features. Hence, our measurements can be best utilized to estimate the range of roughness over the top of the bank rather than a precise value at an individual location. The measured values of velocity and TKE dissipation rate ε were interpolated to a grid with 0.5-m vertical spacing. The bottom boundary layer depth where density changed by 0.01 kg m^{-3} from the near-bottom density was about 4 m from the bottom for nearly 75% of the VMP profiles collected over the bank. The inertial boundary layer is typically less than 20% of the boundary layer depth and is expected to be less than 1 m. Dissipation measurements were averaged over the first 4 m from the bottom (or approximately over the bottom boundary layer), and five sequential profiles were combined, resulting in spacing on the order of 1 km. The maximum likelihood estimator method (Baker and Gibson 1987) was used to calculate the expected value and 95th percentile confidence limits. Velocities were also averaged in time using five adjacent profiles, and any measurements more than 7.5 m above the bottom were discarded. The frictional velocity u_* [(14)] was calculated from ε as described above, and errors are propagated to the new term. The near-bottom mean velocity $\tilde{U}$ was calculated in two different ways: (i) using the smoothed velocity at the deepest available depth (d_0), and (ii) by a linear extrapolation of velocities to 3 m above the bottom using the deepest two bins. These two methods are referred to as $\tilde{U}_1$ and $\tilde{U}_2$, respectively. The two techniques provide a better sense of the range of $\tilde{U}$, as the ship ADCP typically did not measure velocities within the inertial layer, with the deepest bin typically 5–7 m above the bottom. Both versions of $\tilde{U}$ were applied to calculate values of z_0, with errors in z_0 propagated from u_* and $\tilde{U}$. Calculations of C_d [(13)] are based on a reference height at $z_a = 3$ m above the bottom, which lies within the bottom boundary layer. The minimum for z_0 was set to 10^{-3} cm, as this is the value for a muddy bottom (Deacon 1953), and lower values are physically unrealistic.

Habitat composition maps show algal nodules covering most of the bank, with the coral reef zone (55% coverage) over the shallower regions (Fig. 1). The expectation is that the bank will contain a range of values, including both smooth areas and rough (coral coverage) regions. Prior estimates indicate that the roughness lengths over corals are expected to be several centimeters (Rosman and Hench 2011), much larger than what was seen at the moorings located just off and on top of the bank. Calculated roughness lengths [(15)], measured dissipation rates, and bottom velocities along the two transects shown in Fig. 14 contain significant variability, partly due to limited sampling in both space and time. Dissipation, velocity magnitude, and frictional velocity (multiplied by 10) are shown in the first two panels of Fig. 14 for T1 and T2 (the transects highlighted in Figs. 2a,c). The third panel shows two estimates of the roughness length z_0, with 95th percentile confidence levels calculated from the near-bottom velocity $\tilde{U}$ alone (black line) and with the mean and standard deviation of z_0 derived using $\tilde{U}_1$ and $\tilde{U}_2$ (red line). Along both T1 and T2, which pass over the shallow coral zone, the roughness lengths have values between 1 and 10 cm (Fig. 14), as expected over corals (Rosman and Hench 2011).

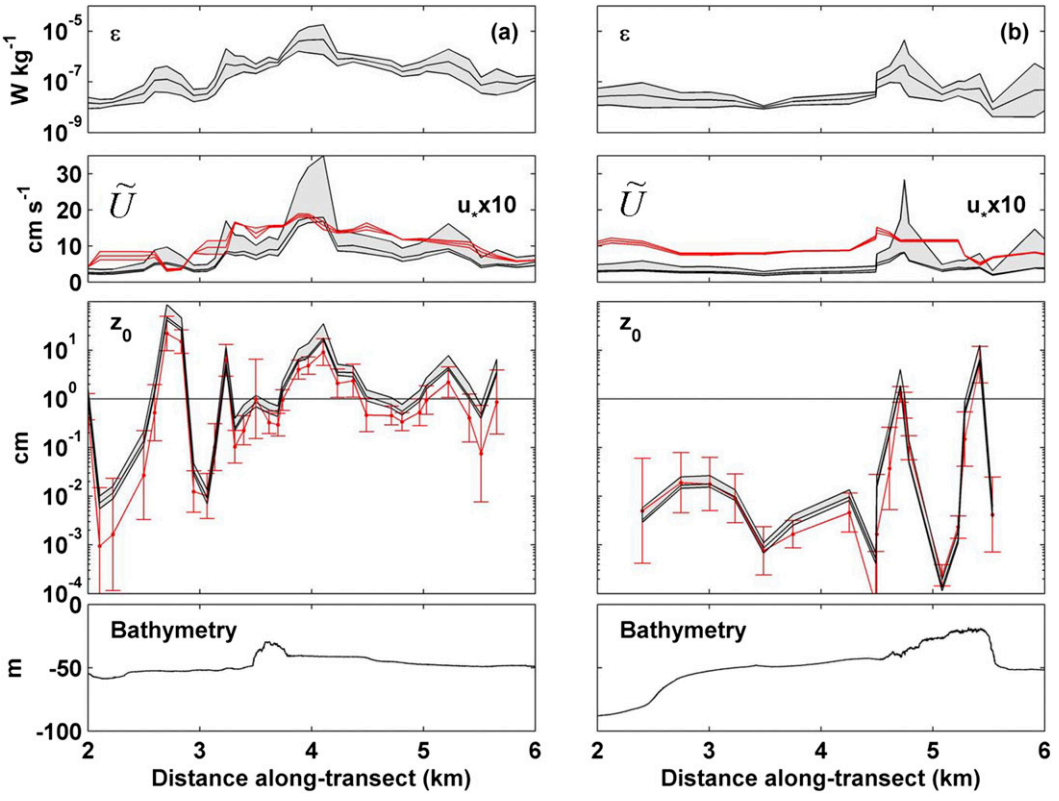

FIG. 14. Near-bottom TKE dissipation rate ε, near-bottom velocity $\tilde{U}$, friction velocity u_* ($\times 10$), roughness length z_0, and bathymetry at transects (a) T1 and (b) T2. The shaded regions in the first three panels are the 95th percentile errors for each parameter. For z_0, both the value calculated using only the near-bottom velocity (black line) and the mean and standard deviation of the three z_0 values obtained using $\tilde{U}_1$ and $\tilde{U}_2$ (red line with error bars) are shown. The horizontal line is at 1 cm, the lowest reported value for coral roughness in prior studies (Rosman and Hench 2011).

The calculated roughness lengths [(15)] and the associated drag coefficients [(13)] over the EFGB vary spatially (Fig. 15). Given the transect range of the ship ADCP, estimates of z_0 and C_d are exclusively over the top and sides of the bank. To get values over the sandy bottom next to the bank, estimates of z_0 at the long-term mooring locations were made using times when the dissipation transects came within approximately 500 m of a mooring. Measured $\tilde{U}$ was 1–5 m off the bottom, depending on the mooring configuration. M4, M5, and M6 had close transects and an ADCP bin within 5 m of the bottom. M5 is near the top the bank, but was placed in an area free of coral in order to avoid damage to the reef. Estimates for z_0 are 0.02 cm at two mooring locations (M4 and M6) and 0.2 cm at the third (M5). Some uncertainty is expected because we do not have dissipation time series at these locations, but the values are consistent with other estimates over a sandy bottom (Reidenbach et al. 2006). Distribution functions of both z_0 and C_d deviate substantially from the Gaussian distribution and are close to the lognormal distribution. The values of z_0 based on 243 estimates varied between 0.001 and 68 cm with an arithmetic mean of 3.62 cm (Figs. 14, 15; Table 2). The values of C_d varied between 1×10^{-3} and 75×10^{-3}, with an arithmetic mean of 6.2×10^{-3} (Fig. 15; Table 2).

The range of frictional regimes over the bank can be seen in Fig. 16, which shows C_d and the roughness Reynolds number Re_*, defined as $\mathrm{Re}_* = z_0 u_*/\nu$. For pipe flows, Re_* shows hydraulically smooth regimes for $\mathrm{Re}_* < 5$ and completely rough regimes for $\mathrm{Re}_* > 70$ (e.g., Schlichting 1962). A drag coefficient of 2×10^{-3} is indicated by a black line, as this is the approximate value at the mooring locations and represents a hydraulically smooth bottom. The measurements comprise both values typical for a smooth bottom as well as values similar to those measured previously over corals (i.e., values of 9–150×10^{-3} found by Reidenbach et al. 2006).

6. Discussion

a. *Form drag, power, and bulk drag coefficient*

Analysis of a 6-month-long time series of pressure over the EFGB revealed that D_{form} was generated by

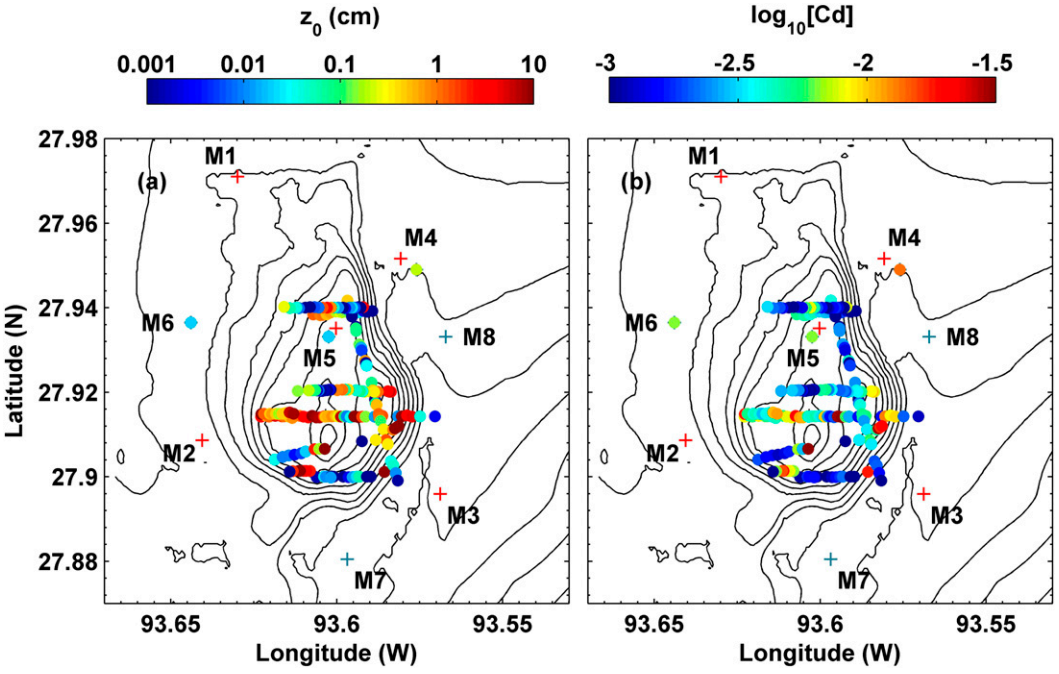

FIG. 15. All values of (a) z_0 (cm) and $\log_{10}$ values of (b) bottom drag coefficient (C_d) over the bank.

multiple time-scale processes. The magnitude of D_{form} at the diurnal tidal band is about 1500 N m^{-1} for tidal velocities of about 3–5 cm s^{-1} (Table 1), and the inertial drag was a significant component of the total form drag for this band. Apart from D_{form} at tidal oscillations, we found large form drags at subtidal bands with time scales of 4–6-, 10–11-, and 16–17-day periods (Figs. 9, 10) for depth-averaged currents less than 10 cm s^{-1}. For these low-frequency bands, the inertial drag was negligible. Values of D_{form} for diurnal tides and 4–17-day oscillations were similar. Form drags resulting from semidiurnal tides are well documented in previous studies (Nash and Moum 2001; Warner et al. 2013), but there are no quantitative estimates of the form drag for subtidal motions such as 4–17-day oscillations observed in the GoM. Our analysis demonstrates that the form drag resulting from low-frequency currents is an important flow retardation mechanism even in the presence of the large frictional drag associated with coral reefs.

The 6-month averaged power removed from the low-frequency motions by the form drag was 85 W m^{-1} (Table 1). Jarosz et al. (2014, manuscript submitted to *J. Geophys. Res.*) computed the along-transect and depth-integrated turbulent kinetic energy dissipation rate E over the bank (transects shown in Fig. 2a), where $E = \rho_0 \iint \varepsilon \, dz \, dx$. The quantity E varied between 6.5 and 40 W m^{-1}, and the space–time-averaged E over seven transects was about 23 W m^{-1}. The short-term estimates of TKE dissipation are a factor of 2–4 smaller than the 6-month averaged P_{form}. These differences are not surprising, since winds and background currents were weak during the IOP. The 6-month averaged bulk drag coefficient C_D over the bank can vary between 0.03 and 0.22, which is 3–35 times larger than the estimated frictional drag coefficient C_d, apart from the fact that the frictional drag coefficient over the bank is also large due to the coral habitats (Tables 1, 2).

b. Parameter dependence and linear theory

We computed the nondimensional parameters h_n, a_n, and K (defined in section 1) by replacing N_0 by N and U_0 by U_U. We noted for flow over the EFGB that h_n (Fig. 17) and K were greater than 1 for most occasions, except for when the stratification became weak and the mixed layer was deep, as observed during late fall frontal passages. Here N is estimated from the 6-h low-pass filtered potential density at 15 and 65 m at S2, and U_U is the 6-h low-pass filtered, upper 50-m, depth-averaged flow speed at

TABLE 2. Bottom roughness z_0 and frictional drag coefficient C_d estimated over the EFGB. Maximum, minimum, arithmetic mean, and median were estimated from 243 observations. The maximum likelihood estimator (MLE) was computed by assuming lognormal distributions for z_0 and C_d, where MLE = $\exp(m + s^2/2)$; m and s are the arithmetic mean and standard deviation of ln(variable) (e.g., Baker and Gibson 1987).

Variable	Minimum	Maximum	Mean	Median	MLE
z_0 (cm)	0.001	68	3.6	0.24	22
C_d	0.001	0.075	0.0062	0.0032	0.0056

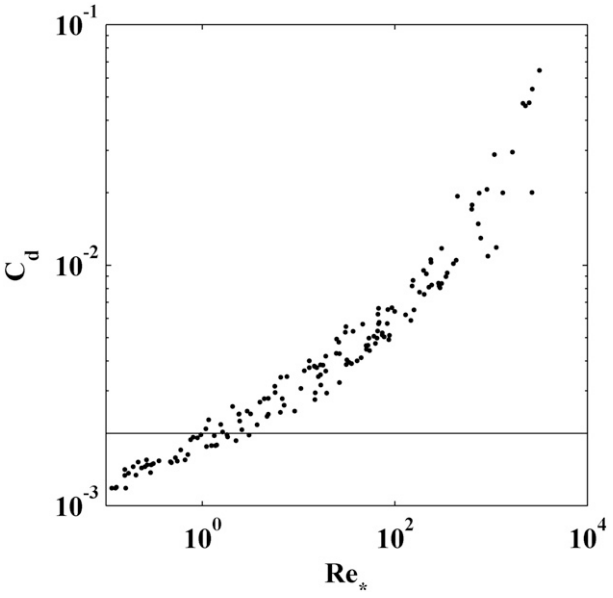

FIG. 16. The term C_d as a function of frictional Reynolds number Re_*. The horizontal line is at 0.002, the approximate value of C_d at the mooring locations.

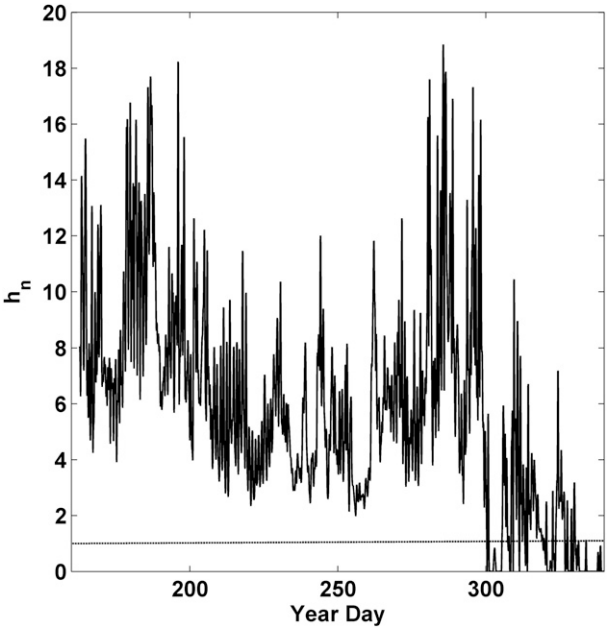

FIG. 17. Nondimensional bank height h_n at M1. Fluctuations less than 10 h were filtered out before plotting. The dashed line represents $h_n = 1$.

M1. For $h_0 = 46$ m, $D = 100$ m, $L = 6$ km, and $a_0 = 1$ km, h_0/L is 0.017 and h_0/D is 0.46. The nondimensional parameters h_n, K, and a_n calculated from the time-averaged velocity U_U and the buoyancy frequency N are about 5.6 ($\pm$3.5), 3.8 ($\pm$2.6), and 125 ($\pm$78), respectively, where the time-averaged U_U and N are 0.15 ($\pm$0.07) m s^{-1}, and 0.023 ($\pm$0.005) s^{-1}, respectively. The standard deviations are given in parentheses. The height parameter h_0/D shows that the bank occupies nearly 50% of the water column, and values of nondimensional parameters ($a_n \gg 1$, $h_n \gg 1$, $K \gg 1$, and $D/L \ll 1$) suggest highly nonlinear, hydrostatic, high drag state flow with upstream blocking (e.g., Baines 1979; Hunt and Snyder 1980; Vosper et al. 1999). The relation $a_n \gg 1$ indicates that the lateral scale of the bank is much larger than the distance traveled by the flow during a buoyancy period.

Garrett and Kunze (2007) have suggested extra parameters including a steepness parameter, $e_n = kh_0[(\omega^2 - f^2)/(N^2 - \omega^2)]^{-1/2}$, and a tidal excursion kU_U/ω for oscillatory flows over the bank with frequency ω ($>f$) and horizontal wavenumber k. For flows over the EFGB, the steepness parameter exists for the K_1 tide with ω_{K1} ($=7.29 \times 10^{-5}$ s^{-1}) $> f$ ($=6.84 \times 10^{-5}$ s^{-1}), $e_n = 10^4$ and $kU_U/\omega_{K1} = 2.0$ for $k = 1/a_0 = 1 \times 10^{-3}$ m^{-1}. The relation $e_n \gg 1$ suggests that the topographic slope is supercritical with respect to the tidal ray slope, and $kU_U/\omega = 2$ suggests that quasi-steady lee waves can be generated in the region.

Formation of hydrostatic lee waves and the associated form drag for $a_n \gg 1$ and $h_n < 1$ have been studied extensively (e.g., Baines 1995). As discussed in section 4e, D_{wave} and D_{form} have similar directions, but the magnitude of D_{wave} is smaller than the measured form drag (Fig. 13). The dynamics of the blocking flow ($h_n \gg 1$) observed here was significantly different from Queney's (1948) nonblocked flow solution. A theoretical description of the flow for $a_n \gg 1$ and $h_n \gg 1$ is not well established. If the wave drag [(16)] can be approximated as the form drag defined in (3) and (4), then drag coefficients are functions of nondimensional parameters such as h_n and h_0/l_0, that is, $C_{DF} = \pi h_n/4$ and $C_D = \pi h_n/4(h_0/l_0)$. Vosper et al. (1999) show that the C_{DF} increases by a factor 3 as h_n increases from 1 to 4 and is consistent with $C_{DF} \approx \pi h_n/4$. This linear relationship between C_{DF} and h_n was explored, but the error bars were large, and no functional form was found.

Jarosz et al. (2014, manuscript submitted to *J. Geophys. Res.*) reported upstream stagnation flow, flow around the bank, vortex formation, and bottom flow reversals on the lee side of the EFGB. They noted that their findings were qualitatively similar to the laboratory experiments (e.g., Baines 1979; Hunt and Snyder 1980; Vosper et al. 1999). The dynamical parameters ($a_n \gg 1$, $h_n \gg 1$, $K \gg 1$, and $D/L \ll 1$) and the observations of Jarosz et al. (2014, manuscript submitted to *J. Geophys. Res.*) suggest that at least part of the measured form drag was caused by pressure anomalies associated with flow separation and vortices generated on the lee side. The strongest flow over the bank was associated with near-inertial waves

(Teague et al. 2013); hence, flow separation and eddy shedding could occur within the inertial cycle on the lee side of the bank (especially over the steep slopes), apart from the low-frequency motions. The Rossby number U_U/fL is about 0.35 ($\pm$0.14) for $U_U = 0.15\,\mathrm{m\,s^{-1}}$, $f = 6.84 \times 10^{-5}\,\mathrm{s^{-1}}$, and $L = 6\,\mathrm{km}$, and therefore rotation can also be a factor in the local dynamics (e.g., Smith 1979).

c. *Frictional drag coefficients associated with corals*

The frictional drag coefficient over the bank is large due to high roughness elements associated with coral reefs. The observations, which were utilized to estimate this coefficient, were made when winds were weak and surface waves were small. Consequently, surface wave–induced bottom currents could not influence the bottom TKE dissipation rate. The estimated roughness lengths reflect the true roughness lengths of small-scale bathymetric features over the EFGB. The coral coverage is not continuous over the bank, and thus z_0 had a range of values from those representing a smooth bottom with a roughness length of 0.001 cm to those for relatively rough regimes with z_0 as high as 68 cm. Nearly ⅓ of our estimates were greater than 1 cm, and the average drag was about 6×10^{-3}. These higher roughness lengths correspond to high drag coefficients and large frictional Reynolds numbers. The impact of high bottom frictional forces can be important because the strength of the bottom boundary layer stress can change lee-wave formation, decrease the form drag, and reduce the overall momentum loss to bottom obstacles/banks compared to a typically assumed free-slip boundary (Skyllingstad and Wijesekera 2004). Pratt (1986) reported that hydraulic controlled flows over straits and sills with friction can alter the dynamics of the flow such as shifting of control points from a sill to downstream locations. Although these modeling studies do not mimic the EFGB observations, the observed large bottom stress over the bank is a factor to consider in the parameterization of the form drag.

7. Summary and conclusions

Hydrographic, velocity, microstructure, and bottom pressure measurements were used to quantify the magnitude and temporal variability of the form drag, roughness lengths, and associated frictional drag coefficients over the EFGB bank. The EFGB is a rough topographic feature located on the Louisiana–Texas shelf approximately 190 km southeast of Galveston, Texas. The EFGB, about 6 km wide and 10 km long, is located at the shelf edge in 100 m of water depth with a peak rising to about 18 m below the sea surface. The area encompassed by the 100-m bathymetric contour of the bank is about 40 $\mathrm{km^2}$. The bank is one of the northernmost tropical coral reefs. The bank includes both coral coverage and sandy bottoms.

Nearly 6-month-long bottom pressure records (June–December 2011) showed significant semidiurnal (M_2) tide, diurnal (K_1 and O_1) tides, and 4–17-day variability over and around the bank. Note that tidal analysis conducted by Teague et al. (2013) showed that the barotropic tidal currents were small (K_1, O_1 speeds $< 5\,\mathrm{cm\,s^{-1}}$) compared to inertial currents that were over $15\,\mathrm{cm\,s^{-1}}$. The M_2 tidal currents were less than $2\,\mathrm{cm\,s^{-1}}$, and the depth-averaged subtidal currents were about 4–9 $\mathrm{cm\,s^{-1}}$.

The estimated form drag from bottom pressure anomalies across the bank showed variability on multiple time scales. Here D_{form} was estimated from three pressure measurements over and around the bank while assuming that the local horizontal pressure gradient was a constant between two observational sites (e.g., Hafner and Smith 1985). It is likely that D_{form} was underestimated by a factor of 2. Therefore, our estimate of D_{form} could be treated as a lower bound of the expected value. The drag resulting from diurnal tidal motions and 4–17-day oscillations had magnitudes of about $2000\,\mathrm{N\,m^{-1}}$. Coefficients of the time-averaged bulk drag C_D ranged from 0.03 to 0.22, which was a factor of 5–35 larger than the averaged frictional drag coefficient (Tables 1, 2). The term P_{form} was estimated as a product of the velocity and the form drag for low-frequency motions. The enumerated power loss per unit length at subtidal motions was about $85\,\mathrm{W\,m^{-1}}$. The total power loss over the bank, $P_{\mathrm{form}}A_0/l_0$, was ~0.37 MW, where $A_0 \approx 40\,\mathrm{km^2}$ and $l_0 = 9\,\mathrm{km}$.

Physical parameters describing the dynamics of flows over the EFGB have a range of values representing a highly nonlinear, hydrostatic flow regime with upstream blocking, where $h_n \gg 1$, $K \gg 1$, and $a_n \sim O(100)$. For these parameters, there is no theoretical prediction of the form drag. The wave drag based on linear theory of the flow over a bank with $h_n \ll 1$ and the measured drag for subtidal flows had similar directions, but the linear theory underpredicted the observations. The quadratic drag law appears to have a better agreement with observations.

Using measurements of the velocity and estimated TKE dissipation rates along multiple transects crossing the bank, the range of roughness lengths z_0 and bottom frictional drag coefficients C_d were computed (Table 2). These measurements of the velocity and dissipation over the bank provide the first estimates of frictional drag coefficients and roughness lengths over the EFGB. Over the top of the bank the bottom roughness lengths encompass those expected for a smooth bottom with z_0 of 0.001 cm as well as higher roughness values over corals. Given that the coral coverage is not continuous, a range of values representing smooth to relatively rough regimes was

expected. The range of z_0 was from 0.001 to 68 cm, with mean and median values of 3.6 and 0.24 cm, respectively (Table 2). Nearly 1/3 of the roughness estimates were greater than 1 cm. The mean and median of the frictional drag coefficient were about 6×10^{-3} and 3×10^{-3}, respectively (Table 2). These findings are comparable with previous measurements over other coral reefs (e.g., Reidenbach et al. 2006).

Large roughness elements can impact the hydraulic flow control as well as coral reef ecology. Locations with coral coverage have increased drag, leading to more turbulence and mixing at these locations relative to regions without corals. This turbulence in turn increases the delivery of nutrients and particulates to the corals. Additionally, it helps to disperse larvae during spawning events, generating a positive feedback cycle that sustains the health of the coral community. The magnitude of the bottom stress over the bank can modify the separation of flow, lee-wave structure and strength of the form drag; hence, it is a factor to consider in the parameterization of the form drag in numerical models. Consequently, our observations and analysis of the hydrographic, velocity, microstructure, and pressure measurements suggest that the EFGB is a ''hot spot'' of mixing on the shelf of GoM. The analysis further demonstrates that the form drag resulting from low-frequency currents over an isolated bank on the continental shelf is an important physical process that must be parameterized to represent a wide range of flow states.

Acknowledgments. This work was sponsored by the Office of Naval Research in an NRL project referred to as Mixing Over Rough Topography (MORT) and by the BOEM in the project referred to as Currents Over Banks (COB) through the Interagency Agreement M10PG00038. Support for James Moum was provided through ONR Grant N00014-09-1-0280. The measurements were made in cooperation with the Flower Garden Banks National Marine Sanctuary, administered by the National Oceanic and Atmospheric Administration (NOAA). Assistance provided by Alexis Lugo-Fernandez of BOEM and Emma Hickerson of NOAA and the crew of the R/V *Pelican* and R/V *Manta* was greatly appreciated.

APPENDIX

Estimation of the Form Drag Based on Numerical Simulations: Sensitivity Study

The form drag over an underwater topographic feature is estimated from bottom pressure fluctuations and a horizontal slope of the bathymetry, as indicated in (1). The accuracy of the estimated drag depends on the number of pressure measurements and the location of the pressure measurements. A sensitivity study was conducted to examine the minimum number of pressure measurements required to calculate a reasonable estimate of the form drag. Here we used numerically simulated pressure fields over a sloping headland, TTP in Puget Sound, Washington, developed by Warner (2012) as part of her Ph.D. dissertation. The TTP model was based on the Regional Ocean Modeling System (ROMS), and details of the model setup is given by Warner (2012). The study helps us to quantify some uncertainties in an estimation of the form drag over the EFGB based on three pressure measurements. The ROMS results are an approximation to the real observations due to numerical limitations given by Warner (2012). It is also noted that the shape and size of TTP are different from the EFGB and that the locations of Ppods during MORT might have missed large pressure fluctuations. Therefore, the results discussed below have more uncertainties than the model results alone.

A time series of modeled bottom pressure anomalies along the TTP ridge was used to compute the form drag based on (1). The spatial resolution of the model was 50.5 m. The ridge is about 2 km wide and is nearly symmetrical (Fig. A1). Gradients of the ridge, perpendicular to the ridge axis, are strongest on the midsections of the ridge with the maximum on the right side and the minimum on the left side. Total pressure anomalies [(8)] including external, internal, and inertial components at three different locations (near bottom and top of the ridge) are shown in Fig. A2.

We computed the form drag using the modeled pressure along the ridge and the measured slope with 50.5-m spatial resolution and referred to it as the complete solution D_0:

$$D_0 = -\sum_{i=1}^{I} (p_B)_i \left(\frac{\partial h}{\partial x}\right)_i \Delta x, \quad \text{and} \quad \Delta x = 50.5\,\text{m}, \qquad \text{(A1)}$$

where I is the total number of pressure measurements used in the integration, and $X_3 - X_1 = I\Delta x = 2.1$ km (Fig. A1). We computed D_{form} by approximating the pressure field based on three pressure measurements at X_1, X_2, and X_3, while mimicking the observational setup over the EFGB during the MORT.

a. Method I

The first estimate was made by using mean values of the pressure and slope over the bank, and the resulting drag is

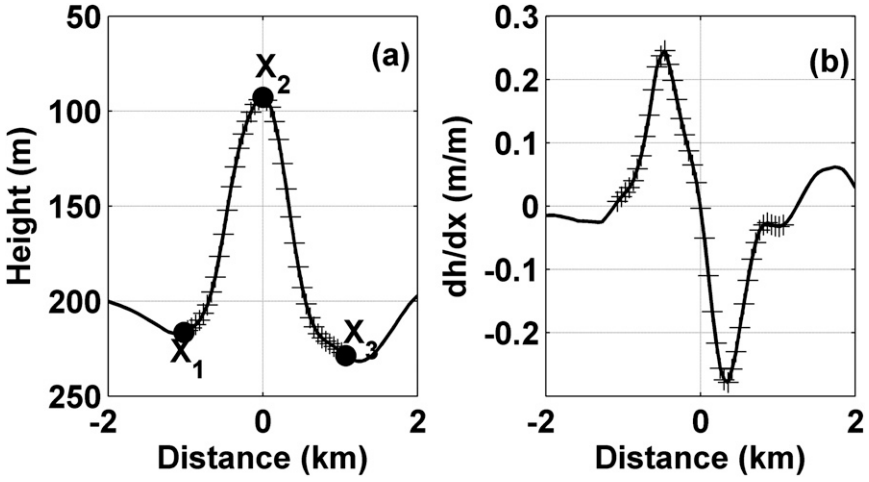

FIG. A1. (a) Cross section of the ridge transect based on the model bathymetry. Spatial resolution is 50.5 m. The crosses are the data points used in the analysis. The bullets represent locations of pressure time series plotted in Fig. A2. (b) Horizontal gradient of ridge topography, dh/dx across the ridge (from Warner 2012).

$$D_1 = -P_{m1}\left\langle\frac{\partial h}{\partial x}\right\rangle_1[\mathrm{X}_2 - \mathrm{X}_1] - P_{m2}\left\langle\frac{\partial h}{\partial x}\right\rangle_2[\mathrm{X}_3 - \mathrm{X}_2], \tag{A2}$$

where $P_{m1} = [p_B(\mathrm{X}_1) + p_B(\mathrm{X}_2)]/2$ and $P_{m2} = [p_B(\mathrm{X}_2) + p_B(\mathrm{X}_3)]/2$. The angle brackets are the spatial means over the slope.

b. Method II

The second approximation assumed that the pressure distribution was linear over the slopes. We interpolated pressure linearly between X_1 and X_2 representing the left side of the bank and pressures between X_2 and X_3 representing the right side of the bank. The resulting drag based on the linearly interpolated bottom pressure p_I with fully resolved bathymetric slope ($\partial h/\partial x$) is

$$D_2 = -\sum_{i=1}^{I}(p_I)_i\left(\frac{\partial h}{\partial x}\right)_i \Delta x. \tag{A3}$$

c. Method III

Here the form drag was approximated by using a mean value of the pressure and the maximum slope over the bank, and the resulting drag is

$$D_3 = -P_{m1}\left|\frac{\partial h}{\partial x}\right|_{\max 1}[\mathrm{X}_2 - \mathrm{X}_1] + P_{m2}\left|\frac{\partial h}{\partial x}\right|_{\max 2}[\mathrm{X}_3 - \mathrm{X}_2], \tag{A4}$$

where $|\partial h/\partial x|_{\max 1}$ and $|\partial h/\partial x|_{\max 2}$ are the maximum slopes of left and right sides of the bank (Fig. 2b).

The estimated drag over the ridge from the three different methods is illustrated in Fig. A3. The drag resulting from all three methods have the same sign, even though the magnitudes of the complete solution (D_0) and method III (D_3) are larger than D_1 [(A2)] and D_2 [(A3)]. The terms D_1 and D_2 have similar magnitudes, but their maximum magnitudes are about 2 times smaller than the maximum of D_0 and D_3 (Fig. A3). However, when averaged over the tidal cycle, both D_1 and D_2 are about 70% of the complete solution D_0.

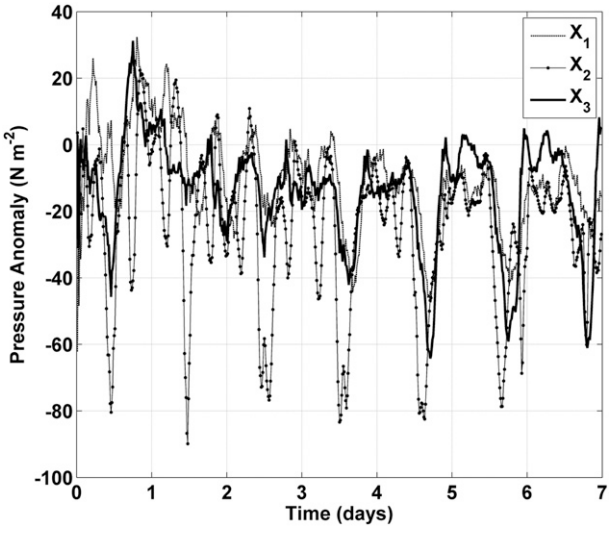

FIG. A2. Dynamic bottom pressure fluctuations at three different locations: X_1, X_2, and X_3. Locations of X_1, X_2, and X3 are marked in bullets in Fig. A1 (from Warner 2012).

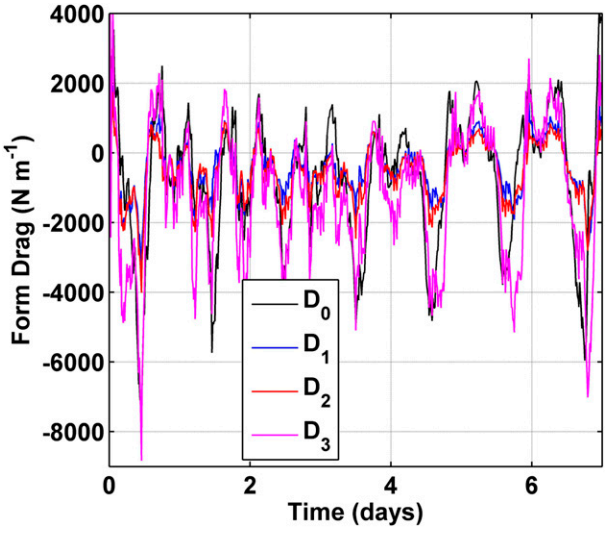

FIG. A3. Estimated pressure drag from four different methods: the complete integration D_0 [(A1)], mean pressure and mean lateral gradient D_1 [(A2)], linearly interpolated solution D_2 [(A3)], and mean pressure and maximum amplitude of lateral gradient, D_3 [(A4)].

There are large variations of the slope across the ridge, and it appears that the slope is an important factor in the computations.

REFERENCES

Baines, P. G., 1979: Observations of stratified flow over two-dimensional obstacles in fluid of finite depth. *Tellus,* **31,** 351–371, doi:10.1111/j.2153-3490.1979.tb00914.x.

——, 1995: *Topographic Effects in Stratified Flows.* Cambridge University Press, 482 pp.

Baker, M. A., and C. H. Gibson, 1987: Sampling turbulence in the stratified ocean: Statistical consequences of strong intermittency. *J. Phys. Oceanogr.,* **17,** 1817–1836, doi:10.1175/1520-0485(1987)017<1817:STITSO>2.0.CO;2.

Bell, T. H., 1975: Topographically generated internal waves in the open ocean. *J. Geophys. Res.,* **80,** 320–327, doi:10.1029/JC080i003p00320.

Blumberg, A. F., and G. L. Mellor, 1987: A description of a three-dimensional coastal ocean circulation model. *The Three Dimensional Coastal Ocean Models,* N. S. Heaps, Ed., Coastal and Estuarine Sciences Series, Vol. 4, Amer. Geophys. Union, 1–16.

Bougeault, P., B. Benech, B. Carissimo, J. Pelon, and E. Richard, 1990: Momentum budget over the Pyrenees: The PYREX experiment. *Bull. Amer. Meteor. Soc.,* **71,** 806–818, doi:10.1175/1520-0477(1990)071<0806:MBOTPT>2.0.CO;2.

Bright, T. J., G. P. Kraemer, G. A. Minnery, and S. T. Viada, 1984: Hermatypes of the Flower Garden Banks, northwestern Gulf of Mexico: A comparison to other western Atlantic reefs. *J. Mar. Sci.,* **34,** 491–476.

Clark, T. L., and M. J. Miller, 1991: Pressure drag and momentum fluxes due to the Alps. II: Representation in large-scale models. *Quart. J. Roy. Meteor. Soc.,* **117,** 527–552, doi:10.1002/qj.49711749906.

Deacon, E. L., 1953: Vertical profiles of mean wind in the surface layers of the atmosphere. *Geophysical Memoirs,* No. 91, H. M. Stationery Office, 63 pp.

Dewey, R. K., and W. R. Crawford, 1988: Bottom stress estimates from vertical dissipation rate profiles on the continental shelf. *J. Phys. Oceanogr.,* **18,** 1167–1177, doi:10.1175/1520-0485(1988)018<1167:BSEFVD>2.0.CO;2.

Donohue, K., P. Hamilton, K. Leaman, R. Leben, M. Prater, D. R. Watts, and E. Waddell, 2006: Exploratory study of deepwater currents in the Gulf of Mexico. Volume II: Technical report. U.S. Department of the Interior Mineral Management Service, OCS Study MMS 2006-074, 408 pp.

——, ——, R. R. Leben, D. R. Watts, and E. Waddell, 2008: Survey of deepwater currents in the northwestern Gulf of Mexico. Volume II: Technical report. U.S. Department of the Interior, Minerals Management Service, OCS Study MMS 2008-031, 364 pp.

Doyle, J. D., and Q. F. Jiang, 2006: Observations and numerical simulations of mountain waves in the presence of directional wind shear. *Quart. J. Roy. Meteor. Soc.,* **132,** 1877–1905, doi:10.1256/qj.05.140.

Durran, D. R., 1986: Another look at downslope wind storms. Part I: The development of analogs to supercritical flow in an infinitely deep, continuously stratified fluid. *J. Atmos. Sci.,* **43,** 2527–2543, doi:10.1175/1520-0469(1986)043<2527:ALADWP>2.0.CO;2.

——, 1990: Mountain waves and downslope winds. *Atmospheric Processes over Complex Terrain, Meteor. Monogr.,* No. 45, Amer. Meteor. Soc., 59–81.

Edwards, K. A., P. MacCready, J. N. Moum, G. Pawlak, J. Klymak, and A. Perlin, 2004: Form drag and mixing due to tidal flow past a sharp point. *J. Phys. Oceanogr.,* **34,** 1297–1312, doi:10.1175/1520-0485(2004)034<1297:FDAMDT>2.0.CO;2.

Firing, E., J. Ranada, and P. Caldwell, cited 1995: CODAS ADCP processing. [Available online at http://currents.soest.hawaii.edu/docs/doc/codas_doc/.]

Garrett, C., and E. Kunze, 2007: Internal tide generation in the deep ocean. *Annu. Rev. Fluid Mech.,* **39,** 57–87, doi:10.1146/annurev.fluid.39.050905.110227.

Gill, A. E., 1982: *Atmosphere–Ocean Dynamics.* Academic Press, 662 pp.

Grant, W. D., and O. S. Madsen, 1982: Movable bed roughness in unsteady oscillatory flow. *J. Geophys. Res.,* **87,** 469–481, doi:10.1029/JC087iC01p00469.

Gregg, M. C., 1987: Diapycnal mixing in the thermocline: A review. *J. Geophys. Res.,* **92,** 5249–5286, doi:10.1029/JC092iC05p05249.

Grubisic, V., and Coauthors, 2008: The terrain-induced rotor experiment: A field campaign overview including observational highlights. *Bull. Amer. Meteor. Soc.,* **89,** 1513–1533, doi:10.1175/2008BAMS2487.1.

Hafner, T. A., and R. B. Smith, 1985: Pressure drag on the European Alps in relation to synoptic events. *J. Atmos. Sci.,* **42,** 562–575, doi:10.1175/1520-0469(1985)042<0562:PDOTEA>2.0.CO;2.

Hodur, R. M., 1997: The Naval Research Laboratory's Coupled Ocean/Atmosphere Mesoscale Prediction System (COAMPS). *Mon. Wea. Rev.,* **125,** 1414–1430, doi:10.1175/1520-0493(1997)125<1414:TNRLSC>2.0.CO;2.

Hunt, J. C. R., and W. H. Snyder, 1980: Experiments on stably and neutrally stratified flow over a model three-dimensional hill. *J. Fluid Mech.,* **96,** 671–704, doi:10.1017/S0022112080002303.

Jayne, S. R., and L. C. St. Laurent, 2001: Parameterizing tidal dissipation over rough topography. *Geophys. Res. Lett.,* **28,** 811–814, doi:10.1029/2000GL012044.

Khatiwala, S., 2003: Generation of internal tides in an ocean of finite depth: Analytical and numerical calculations. *Deep-Sea Res. I,* **50,** 3–21, doi:10.1016/S0967-0637(02)00132-2.

Kim, Y.-J., and A. Arakawa, 1995: Improvement of orographic gravity parameterization using a mesoscale gravity wave model. *J. Atmos. Sci.,* **52,** 1875–1902, doi:10.1175/1520-0469(1995)052<1875:IOOGWP>2.0.CO;2.

——, S. D. Eckermann, and H.-Y. Chun, 2003: An overview of the past, present and future of gravity-wave drag parameterization for numerical climate and weather prediction models: Survey article. *Atmos.–Ocean,* **41,** 65–98, doi:10.3137/ao.410105.

Lamb, K. G., 1994: Numerical experiments of internal wave generation by strong tidal flow across a finite amplitude bank edge. *J. Geophys. Res.,* **99,** 843–864, doi:10.1029/93JC02514.

Legg, S., and K. M. H. Huijts, 2006: Preliminary simulations of internal waves and mixing generated by finite amplitude tidal flow over isolated topography. *Deep-Sea Res. II,* **53,** 140–156, doi:10.1016/j.dsr2.2005.09.014.

Long, R. R., 1955: Some aspects of the flow of stratified fluids. *Tellus,* **7,** 341–357, doi:10.1111/j.2153-3490.1955.tb01171.x.

Lott, F., and M. J. Miller, 1997: A new subgrid-scale orographic drag parameterization: Its formulation and testing. *Quart. J. Roy. Meteor. Soc.,* **123,** 101–127, doi:10.1002/qj.49712353704.

McCabe, R., P. MacCready, and G. Pawlak, 2006: Form drag due to flow separation at a headland. *J. Phys. Oceanogr.,* **36,** 2136–2152, doi:10.1175/JPO2966.1.

Minnery, G. A., 1990: Crustose coralline algae from the Flower Garden Banks, northwestern Gulf of Mexico; Controls on distribution and growth morphology. *J. Sediment. Res.,* **60,** 992–1007, doi:10.1306/D4267663-2B26-11D7-8648000102C1865D.

Moum, J. N., and J. D. Nash, 2000: Topographically induced drag and mixing at a small bank on the continental shelf. *J. Phys. Oceanogr.,* **30,** 2049–2054, doi:10.1175/1520-0485(2000)030<2049:TIDAMA>2.0.CO;2.

——, and W. D. Smyth, 2006: The pressure disturbance of a nonlinear internal wave train. *J. Fluid Mech.,* **558,** 153–177, doi:10.1017/S0022112006000036.

——, and J. D. Nash, 2008: Seafloor pressure measurements of nonlinear internal waves. *J. Phys. Oceanogr.,* **38,** 481–491, doi:10.1175/2007JPO3736.1.

Nakamura, T., T. Awaji, T. Hatayama, K. Akitomo, and T. Takizawa, 2000: The generation of large-amplitude unsteady lee waves by subinertial K1 tidal flow: A possible mixing mechanism in the Kuril Straits. *J. Phys. Oceanogr.,* **30,** 1601–1621, doi:10.1175/1520-0485(2000)030<1601:TGOLAU>2.0.CO;2.

Nash, J. D., and J. N. Moum, 2001: Internal hydraulic flows on the continental shelf: High drag states over a small bank. *J. Geophys. Res.,* **106,** 4593–4612, doi:10.1029/1999JC000183.

Nikuradse, J., 1950: Stromungsgesetz in rauhren rohren (Laws of flow in rough pipes). NACA Tech. Memo. 1292, 63 pp. [Available online at http://www.hach.ulg.ac.be/cms/en/system/files/Nikuardse%2520trad%2520NASA.pdf.]

Nikurashin, M., and R. Ferrari, 2011: Global energy conversion rate from geostrophic flows into internal lee waves in the deep ocean. *Geophys. Res. Lett.,* **38,** L08610, doi:10.1029/2011GL046576.

Oke, P. R., J. S. Allen, R. N. Miller, G. D. Egbert, and P. M. Kosro, 2002: Assimilation of surface velocity data into a primitive equation coastal ocean model. *J. Geophys. Res.,* **107,** 3122–3147, doi:10.1029/2000JC000511.

Olafsson, H., and P. Bougeault, 1996: Nonlinear flows past an elliptic mountain ridge. *J. Atmos. Sci.,* **53,** 2465–2489, doi:10.1175/1520-0469(1996)053<2465:NFPAEM>2.0.CO;2.

Pawlak, G., P. MacCready, K. A. Edwards, and R. McCabe, 2003: Observations on the evolution of tidal vorticity at a stratified deep water headland. *Geophys. Res. Lett.,* **30,** 2234, doi:10.1029/2003GL018092.

Perkins, H., F. De Strobel, and L. Gauldesi, 2000: The Barny Sentinel trawl-resistant ADCP bottom mount: Design, testing, and application. *IEEE J. Oceanic Eng.,* **25,** 430–436, doi:10.1109/48.895350.

Polzin, K. L., J. M. Toole, J. R. Ledwell, and R. W. Schmitt, 1997: Spatial variability of turbulent mixing in the abyssal ocean. *Science,* **276,** 93–96, doi:10.1126/science.276.5309.93.

Pratt, L. J., 1986: Hydraulic control of sill flow with bottom friction. *J. Phys. Oceanogr.,* **16,** 1970–1980, doi:10.1175/1520-0485(1986)016<1970:HCOSFW>2.0.CO;2.

Queney, P., 1948: The problem of air flow over mountains: A summary of theoretical studies. *Bull. Amer. Meteor. Soc.,* **29,** 16–26.

Reidenbach, M. A., S. G. Monismith, J. R. Koseff, G. Yahel, and A. Genin, 2006: Boundary layer turbulence and flow structure over a fringing coral reef. *Limnol. Oceanogr.,* **51,** 1956–1968, doi:10.4319/lo.2006.51.5.1956.

Rosman, J. H., and J. L. Hench, 2011: A framework for understanding drag parameterizations for coral reefs. *J. Geophys. Res.,* **116,** C08025, doi:10.1029/2010JC006892.

Schlichting, H., 1962: *Boundary Layer Theory.* 6th ed. McGraw-Hill, 817 pp.

Seim, K. S., I. Fer, and H. Avlesen, 2012: Stratified flow over complex topography: A model study of the bottom drag and associated mixing. *Cont. Shelf Res.,* **34,** 41–52, doi:10.1016/j.csr.2011.11.016.

Skyllingstad, E. D., and H. W. Wijesekera, 2004: Large-eddy simulation of flow over two-dimensional obstacles: High drag states and mixing. *J. Phys. Oceanogr.,* **34,** 94–112, doi:10.1175/1520-0485(2004)034<0094:LSOFOT>2.0.CO;2.

Smith, R. B., 1978: A measurement of mountain drag. *J. Atmos. Sci.,* **35,** 1644–1654, doi:10.1175/1520-0469(1978)035<1644:AMOMD>2.0.CO;2.

——, 1979: The influence of the earth's rotation on mountain wave drag. *J. Atmos. Sci.,* **36,** 177–180, doi:10.1175/1520-0469(1979)036<0177:TIOTER>2.0.CO;2.

——, 1980: Linear theory of stratified hydrostatic flow past an isolated mountain. *Tellus,* **32,** 348–364, doi:10.1111/j.2153-3490.1980.tb00962.x.

——, 1989: Hydrostatic airflow over mountains. *Advances in Geophysics,* Vol. 31, Academic Press, 1–41, doi:10.1016/S0065-2687(08)60052-7.

Stull, R. B., 1988: *An Introduction to Boundary Layer Meteorology.* Kluwer Academic Publishers, 666 pp.

Teague, W. J., H. W. Wijesekera, E. Jarosz, D. B. Fribance, A. Lugo-Fernández, and Z. R. Hallock, 2013: Current and hydrographic conditions at the East Flower Garden Bank in 2011. *Cont. Shelf Res.,* **63,** 43–58, doi:10.1016/j.csr.2013.04.039.

Tennekes, H., and J. L. Lumley, 1972: *A First Course in Turbulence.* MIT Press, 300 pp.

Vosper, S. B., I. P. Castro, W. H. Snyder, and S. D. Mobbs, 1999: Experimental studies of strongly stratified flow past three-dimensional orography. *J. Fluid Mech.,* **390,** 223–249, doi:10.1017/S0022112099005133.

Warner, S. J., 2012: Using bottom pressure to quantify tidal form drag on a sloping headland. Ph.D. thesis, University of Washington, 131 pp.

——, and P. MacCready, 2009: Dissecting the pressure field in tidal flow past a headland: When is form drag

''real''? *J. Phys. Oceanogr.,* **39,** 2971–2984, doi:10.1175/2009JPO4173.1.

——, ——, J. N. Moum, and J. D. Nash, 2013: Measurement of tidal form drag using seafloor pressure sensors. *J. Phys. Oceanogr.,* **43,** 1150–1172, doi:10.1175/JPO-D-12-0163.1.

Wijesekera, H. W., D. W. Wang, W. J. Teague, and E. Jarosz, 2010: High sea-floor stress induced by extreme hurricane waves. *Geophys. Res. Lett.,* **37,** L11604, doi:10.1029/2010GL043124.

——, ——, ——, ——, W. E. Rogers, D. B. Fribance, and J. N. Moum, 2013: Surface wave effects on high-frequency currents over a shelf edge bank. *J. Phys. Oceanogr.,* **43,** 1627–1647, doi:10.1175/JPO-D-12-0197.1.

Wolk, F., H. Yamazaki, L. Seuront, and R. G. Lueck, 2002: A new free-fall profiler for measuring biophysical microstructure. *J. Atmos. Oceanic Technol.,* **19,** 780–793, doi:10.1175/1520-0426(2002)019<0780:ANFFPF>2.0.CO;2.

Wood, N., A. R. Brown, and F. E. Hewer, 2001: Parameterizing the effects of orography on the boundary layer: An alternative to effective roughness lengths. *Quart. J. Roy. Meteor. Soc.,* **127,** 759–777, doi:10.1002/qj.49712757303.